PHILOSOPHICAL TRANSACTIONS OF THE ROYAL SOCIETY A MATHEMATICAL, PHYSICAL & ENGINEERING SCIENCES

# On Surface-Generated Ambient Noise in an upward Refracting Ocean

M. J. Buckingham

*Phil. Trans. R. Soc. Lond. A* 1994 **346**, 321-352
doi: 10.1098/rsta.1994.0024

# On surface-generated ambient noise in an upward refracting ocean

By M. J. Buckingham

*Marine Physical Laboratory, Scripps Institution of Oceanography La Jolla, CA 92093, U.S.A. and Institute of Sound and Vibration Research, The University, Southampton SO9 5NH, U.K.*

## Contents



Naturally generated ambient noise in the ocean is created by breaking waves, spray and precipitation. Each of these mechanisms produces a pulse of sound that propagates down into the depths of the ocean, and the superposition of all such pulses from across the whole sea surface constitutes the ambient noise field. Since the noise is a stochastic phenomenon, its properties are described in terms of statistical quantities, the most useful being the power spectral density at a point and the cross-spectral density between two points in the field. If these second-order statistical measures are independent of absolute position, the noise field is said to be spatially homogeneous.

In the rare case of an isovelocity, deep ocean, the noise field at depths greater than a wavelength or so beneath the surface is spatially homogeneous, consisting of a random superposition of plane waves. A non-uniform sound speed profile, however, introduces wave-front curvature which modifies the situation significantly: the noise exhibits strong spatial homogeneity over length scales that are comparable with the apertures of typical acoustic arrays. Apart from the implications with regard to

*Phil. Trans. R. Soc. Lond.* A (1994) **346**, 321–352
*Printed in Great Britain*

array performance, this is important in connection with certain aspects of acoustical oceanography, whereby information on the oceanographic environment is extracted from the noise field (Buckingham *et al.* 1992). Such information is accessible only if the structure of the noise field is well understood.

The problem lies in determining the spatial and spectral properties of the noise in a profile. Fundamental to the noise analysis is the Green's function for the channel, which characterizes the propagation conditions; and yet for most non-uniform sound speed profiles the analysis of the Green's function is intractable. However, there is one profile, designated the inverse-square profile, for which a complete, exact solution for the field has been developed (Buckingham 1991). The inverse-square profile is monotonic increasing with depth, giving rise to upward refractive propagation. Such a profile is found in several ocean environments: the polar oceans, where the temperature and hence the sound speed show a minimum at the surface; the mixed surface layer, extending to a depth of order 100 m in the open ocean; and the ocean-surface bubble layer, occupying the first ten metres or so beneath the surface.

An analysis of the noise field in the presence of an inverse square profile, based on the solution for the Green's function, shows that the cross-spectral density of the noise in the vertical consists of three components: a normal mode sum, representing noise originating largely in distant sources; a direct path contribution, from sources that are more or less overhead; and a near-surface term that is negligible at depths greater than a wavelength. In the theoretical noise spectrum, the normal mode and direct path components are prominent, dominating, respectively, at low and high frequencies. The cross-over frequency depends on the parameters of the profile and attenuation in the medium, but for polar oceans is in the region of several hundred hertz. At a much lower frequency, around 10 Hz, where the polar profile ceases to support normal mode propagation, a minimum appears in the theoretical spectrum. This is the result of a very rapid fall off in the normal mode component of the noise and a slow rise of the direct path component with decreasing frequency.

Each of the three components of the vertical cross-spectral density exhibits strong spatial inhomogeneity. This is exemplified by the dramatic dependence of the cross-spectrum on both the mean depth of the sensors and frequency. Although such behaviour adds complexity to the structure of the noise field, this could be advantageous since it allows the possibility of performing inversions on noise cross-spectral data to determine properties of the medium.

Recent measurements of low-frequency (50–2000 Hz) and very low-frequency (5–200 Hz) ambient noise spectra in the marginal ice zone of the Greenland Sea, where the sound speed profile is of the inverse-square form, have been compared with the predictions of the new noise theory. There is evidence in the measured spectra that both the normal mode and direct path components of the noise are present with the predicted relative levels. A minimum around 10 Hz is a ubiquitous feature of the VLF spectra, and the LF spectra show a change of slope close to 400 Hz, both of which are in accord with the theory. Along the ice edge a highly non-uniform (spatial) distribution of energetic sources is known to be present, whose effects in the observed spectra are consistent with arguments developed from the inverse-square noise analysis.

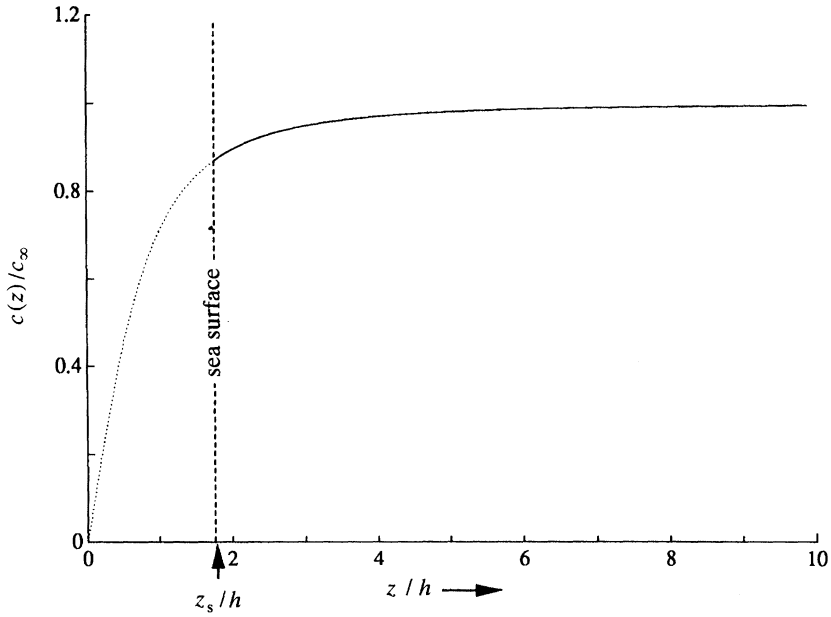


Figure 1. The upward refracting inverse-square profile, with depth normalized to the profile parameter $h$ and sound speed normalized to the asymptotic value $c_\infty$.

## 1. Introduction

Several sea-surface processes, notably wave breaking and precipitation, generate pulses of sound which propagate down into the depths of the ocean. At any point in the ocean, the superposition of all such transient acoustic arrivals from everywhere on the sea surface constitutes the natural, sea-surface generated ambient noise field at that point. Other sources of sound in the ocean, including surface shipping, offshore drilling activities and marine mammals, also contribute to the ambient noise field (Knudsen *et al.* 1948; Wenz 1962; Urick 1983). Such sources are more localized than the natural surface processes and are excluded from the following discussion, which concentrates on the ambient noise field generated by widely distributed natural sea-surface sources.

Considerable attention has been paid to the detailed physical mechanisms whereby sea-surface sources produce sound. Two recent conferences have addressed the issue, one held at Lerici, Italy, in June 1987 (Kerman 1988) and the second at Downing College, Cambridge, U.K., in July 1990 (Kerman 1993). There is now little doubt that oscillating bubbles, created by waves and other processes, are responsible for much of the sound naturally generated at the sea surface. This conclusion is consistent with early work by Minnaert (1933), who was the first to establish, from a series of elegant experiments in which individual air bubbles were released from an underwater nozzle, that a bubble oscillating in the radial 'breathing' mode is a very efficient radiator of sound.

By comparison with the efforts applied to understanding sea-surface sources, relatively little has been done in the way of modelling the effects of the acoustic propagation conditions on the noise field. Cron & Sherman (1962, 1965) developed a model for the spatial coherence of surface-generated noise in a semi-infinite *isovelocity* ocean; and Buckingham (1980), 1981) derived the spatial coherence of the noise in

a shallow isovelocity channel overlying a fast fluid sediment (i.e. a Pekeris (1948) channel). It transpires from this analysis that the noise in shallow water exhibits a modal structure, with the vertical directional density function consisting of discrete noise 'rays' whose grazing angles match those of the eigenrays associated with the modes. Buckingham (1985) subsequently extended his shallow-water arguments to the case of ambient noise in a wedge-shaped isovelocity ocean with pressure-release boundaries.

A theoretical treatment of the cross-spectral density of ambient noise in the presence of a non-uniform sound speed profile was developed by Kuperman & Ingenito (1980). Their expression for the cross-spectral density of the noise at two points in the field, derived from a wave-theoretical argument, is formulated as an integral involving the product of two Green's functions. This integral form is valid for the case of a stratified ocean, in which the sound speed profile may vary with depth but not horizontal range. Kuperman & Ingenito (1980) evaluate their integral numerically, using a fast field program (FFP), and show that the sound speed profile can strongly influence the spatial coherence of the noise. It is also evident from their results that, in general, the ambient noise field in an ocean with a non-uniform profile is spatially inhomogeneous, showing second-order statistical measures that depend on the absolute position at which they are observed.

In the present work, an analytical model giving the vertical coherence of surface-generated ambient noise is developed for a semi-infinite, horizontally stratified ocean with an upward refracting, inverse-square sound speed profile. Such a profile, illustrated in figure 1, is described by the expression

$$c^{-2}(z) = c_\infty^{-2}\{1 + h^2/z^2\}, \quad \text{for} \quad z \geqslant z_s > 0, \tag{1}$$

where $c_\infty$ is the asymptotic sound speed approached in the limit of infinite depth, $h$ is a parameter which specifies the effective depth of the profile in terms of the number of modes that it supports, and $c(z)$ is the sound speed at depth $z$ measured from an origin at a distance $z_s$ above the surface. (The origin of the depth coordinate, $z$, is placed above the surface to prevent the sound speed from falling to zero on the surface.) For a given value of $c_\infty$, prescribed values of the sound speed and sound speed gradient at the surface may be achieved by a judicious choice of $h$ and $z_s$. The inverse-square profile, which is monotonic increasing with depth, is representative of the polar oceans (Kuperman 1988), the surface sound channel, and the bubble layer formed immediately below the sea surface by the action of breaking waves (Farmer & Vagle 1989).

An important component of any ambient noise model is the Green's function for the acoustic field in the channel. Recently, Buckingham (1991), referred to hereafter as I, derived the Green's function for the inverse-square profile by applying two Hankel transforms (over horizontal range and depth) to the Helmholtz equation. His final expression for the field consists of a sum of normal modes plus a branch line integral. An alternative formulation of this solution, derived as an intermediate step in I, is the integral form

$$G = \tfrac{1}{8}\mathrm{j}\sqrt{(zz')}\int_0^\infty p\,\frac{H_\mu^{(1)}(\eta z)}{H_\mu^{(1)}(\eta z_s)}[H_\mu^{(2)}(\eta z')\,H_\mu^{(1)}(\eta z_s) - H_\mu^{(2)}(\eta z_s)\,H_\mu^{(1)}(\eta z')]\,J_0(pr)\,\mathrm{d}p,$$

$$\text{for} \quad z \geqslant z', \tag{2}$$

where $G$ is the harmonic velocity potential (with source strength of unity), $z$ and $z'$

are the depths of the receiver and source below the origin (not the sea surface), $r$ is horizontal range between source and receiver, $\mathrm{j} = \sqrt{-1}$, and the integration variable $p$ is the horizontal wavenumber. The functions $J_0(.)$ and $H_\mu^{(1,2)}(.)$ are, respectively, the Bessel function of the first kind of order zero and the Hankel functions of the first and second kind of order $\mu$; and the two variables $\eta$ and $\mu$ are defined as follows:

$$\eta = \sqrt{(k_\infty^2 - p^2)}, \tag{3}$$

$$\mu = \sqrt{(\tfrac{1}{4} - k_\infty^2 h^2)}, \tag{4}$$

where

$$k_\infty = \omega / c_\infty \tag{5}$$

is the wavenumber at infinite depth and $\omega$ is angular frequency. The solution in (2) satisfies reciprocity, since $z$ and $z'$ are interchanged for a source/receiver configuration such that $z < z'$ (which is not relevant to the analysis of surface-generated noise).

The expression in (2) forms the basis of the following ambient noise analysis. To begin, a brief introduction to the statistical properties of random pulse trains is given in §2, followed by an analysis of the vertical cross-spectral density function of noise in the inverse-square profile in §3, §4. The theory is evaluated in §5 for the marginal ice zone (MIZ) of the Greenland Sea, where, with an appropriate choice of parameters, the observed sound speed profile is accurately fitted by the inverse-square form. A comparison of the theoretical spectra with measured very-low-frequency (< 200 Hz) and low-frequency (50 Hz to 2 kHz) noise spectra from the MIZ is made in §6, where several features observed in the experimental spectra are interpreted on the basis of the theory.

## 2. Random pulse trains

Ambient noise in the ocean, like many other stochastic processes, originates in a very large number of independent discrete random 'events'. In the case of surface-generated oceanic noise, each event could be the breaking of a wave, which produces a bubble cloud and an associated acoustic signature. The superposition of all such acoustic pulses from the whole sea surface constitutes the surface-generated ambient noise field in the ocean. Over an observation interval that is shorter than the timescale of changes in sea surface conditions (arising, for example, from a varying wind vector), such a wave train is statistically stationary, with well-established second-order statistical measures.

Suppose that the acoustic arrival at a receiver from a single event within an elemental surface area $\mathrm{d}A$ is described by a pulse shape function $g(t)$, where causality is satisfied by requirement that $g(t) = 0$ when $t < 0$. It is convenient to assume that all the sources are point impulses (i.e. delta functions in space and time), in which case $g(t)$ is the Green's function of the field at the receiver. Because the profile is dispersive, the pulse arrivals at the receiver undergo some degree of broadening, that is, $g(t)$ is not a delta function. Since all events occurring within $\mathrm{d}A$ share a common propagation path, they generate a noise wave-form at the receiver given by the random superposition

$$x(t) = \sum_{k=1}^{K} a_k g(t - t_k), \tag{6}$$

where $a_k$ and $t_k$ are the amplitude and time of arrival, respectively, of the $k$th pulse, and $K$ is the number of pulses arriving within the observation interval $T$. The




PHILOSOPHICAL TRANSACTIONS OF THE ROYAL SOCIETY A MATHEMATICAL, PHYSICAL & ENGINEERING SCIENCES

statistical properties of the random pulse train $x(t)$ are derived on the assumptions that the summation converges and that the pulse shape function takes appreciable values for a time that is very much less than the observation time, $T$.

Since the pulses occur randomly, the pulse arrivals are Poisson distributed in time with a probability density function equal to $1/T$. It follows (Buckingham 1983) that the (unilateral) power spectral density of $x(t)$ from the element of surface area $\mathrm{d}A$ is

$$\mathrm{d}\langle S(\omega)\rangle = 2\rho\langle a^2\rangle\,|G(\mathrm{j}\omega)|^2\,\mathrm{d}A, \tag{7}$$

where the symbol $\langle . \rangle$ denotes an ensemble average, $\langle a^2\rangle$ is the mean-square value of the pulse amplitudes (the $a_k$ in (6)), $G(\mathrm{j}\omega)$ is the Fourier transform of the Green's function $g(t)$, $\rho$ is the mean rate of events per unit area, and

$$\rho\,\mathrm{d}A = \lim_{T\to\infty}(K/T). \tag{8}$$

Equation (7), known as Carson's theorem (Rice 1944, 1945), indicates that, apart from a scaling factor, the spectrum of the random pulse train $x(t)$ is just the spectrum of the deterministic Green's function $g(t)$. It is implicit in (7) that the process has a zero mean, otherwise a delta function at zero frequency would be included as an additive term on the right.

Carson's theorem is easily generalized to give the cross-spectral density between the noise fluctuations at a pair of sensors due to random events occurring within the elemental surface area $\mathrm{d}A$. If, from the same event, $g_1(t)$ and $g_2(t)$ are the Green's functions at receivers 1 and 2 (figure 2), then the corresponding noise wave forms at the two receivers due to the random succession of events within $\mathrm{d}A$ are given by the superpositions

$$x_1(t) = \sum_{k=1}^{K} a_k\, g_1(t-t_k) \tag{9}$$

and

$$x_2(t) = \sum_{k=1}^{K} a_k\, g_2(t-t_k). \tag{10}$$

Although the pulse arrivals $g_1(t)$ and $g_2(t)$ have a common source, they are not necessarily the same since receivers 1 and 2 lie on different propagation paths; but the causal connection ensures that a one-to-one correspondence exists between the pulses in $x_1(t)$ and $x_2(t)$. This latter condition allows the cross-spectral density between the random pulse trains $x_1(t)$ and $x_2(t)$ to be written as

$$\mathrm{d}\langle S_{12}\rangle = 2\rho\langle a^2\rangle\, G_1(\mathrm{j}\omega)\, G_2^*(\mathrm{j}\omega)\,\mathrm{d}A, \tag{11}$$

where $G_i(\mathrm{j}\omega)$ is the Fourier transform of $g_i(t)$, $i = 1, 2$, $\rho$ is the mean rate of pulses per unit area, and the asterisk denotes complex conjugation. Obviously, (7) is a special case of (11) and we shall refer to both as Carson's theorem.

The cross-spectral density of the total noise field at the two sensors is obtained by integrating (11) over the sea surface:

$$\langle S_{12}\rangle = 2\rho\langle a^2\rangle \int_A G_1(\mathrm{j}\omega)\, G_2^*(\mathrm{j}\omega)\,\mathrm{d}A, \tag{12}$$

and the (complex) coherence function, $\Gamma_{12}$, is defined as

$$\Gamma_{12} = \langle S_{12}\rangle / [\langle S_{11}\rangle\,\langle S_{22}\rangle]^{\frac{1}{2}}. \tag{13}$$

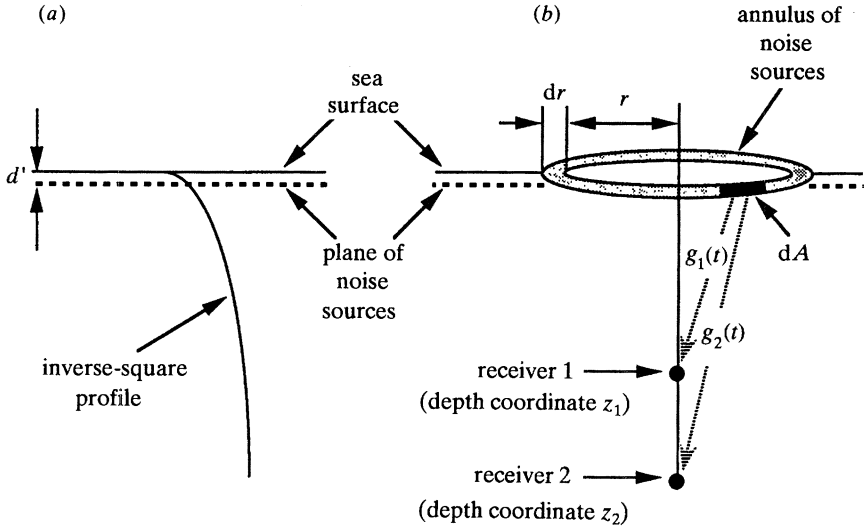


Figure 2. Geometry for the problem of noise in an inverse-square ocean. (*a*) Inverse-square profile. (*b*) Two vertically aligned sensors centred on an annulus of surface noise sources. The Green's functions $g_1(t)$ and $g_2(t)$ represent, respectively, the propagation from a single source within d$A$ to receivers 1 and 2. The hatching on the arrows indicates that in general the propagation is not along straight-line paths.

In reality the surface sources are not impulsive but possess some source strength function that is characteristic of the source mechanism itself. The cross-spectral density, $\langle S_{12} \rangle$, should therefore be modified, but only by a factor representing the source spectrum, and this factor would cancel in (13) leaving the coherence function unaffected.

For two vertically separated sensors in plane-wave, spatially homogeneous noise, the coherence function is related to the directional density function (i.e. the noise power per unit solid angle) through a Fourier transform relationship (Cox 1973); but for spatially inhomogeneous noise fields, as found in an ocean with an inverse-square profile, no such simple connection exists between spatial coherence and noise directionality. Indeed, spatially inhomogeneous noise fields show no unique directional density function, rendering the concept of directionality almost meaningless.

## 3. Theory: noise in the inverse-square profile

To derive the cross-spectral density of surface-generated ambient noise at two vertically aligned sensors in an inverse-square ocean we choose a cylindrical coordinate system, with the axis vertical and passing through both sensors. The origin of the coordinate system is set at a distance $z_s$ above the surface. Immediately below the surface, a random distribution of point, transient sources is located on a horizontal plane whose $z$-coordinate is equal to $z'$. Thus, the depth of the sources is $d' = (z' - z_s)$ (figure 2), which is small compared with all other dimensions in the problem. With little loss of generality, we shall assume that all the source strength functions are an identical shape.

By virtue of the azimuthal symmetry of the problem, the arrivals at a given receiver from all the sources within an annulus on the surface of radius $r$ and thickness d$r$ (figure 2) possess the same Green's function, and hence the surface

integral in Carson's theorem (equation (12)) for the cross-spectral density immediately reduces to a single integral over range:

$$\langle S_{12}(\omega, z_1, z_2)\rangle = 4\pi\rho Q(\omega)\int_0^\infty rG_1(\omega)\,G_2^*(\omega)\,\mathrm{d}r, \tag{14}$$

where $z_1$ and $z_2$ are the depth coordinates of the two receivers, and the spectrum of the sources, $Q(\omega)$, is now included explicitly in the formulation. (If the sources were to generate a variety of acoustic pulse shapes, then $Q(\omega)$ would represent an appropriately weighted average source spectrum.) The Green's functions $G_1$ and $G_2$ are given by the expression in (2) evaluated at the two sensor depths, $z_1$ and $z_2$:

$$G_i(\omega) = \tfrac{1}{8}\mathrm{j}\sqrt{(zz')}\int_0^\infty pS_\mu(\eta, z_i)\,J_0(pr)\,\mathrm{d}p, \quad i = 1, 2, \tag{15}$$

where
$$S_\mu(\eta, z_i) = \frac{H_\mu^{(1)}(\eta z_i)}{H_\mu^{(1)}(\eta z_s)}[H_\mu^{(2)}(\eta z')\,H_\mu^{(1)}(\eta z_s) - H_\mu^{(2)}(\eta z_s)\,H_\mu^{(1)}(\eta z')]. \tag{16}$$

Since the sources lie very close to the surface, a significant simplification can be achieved by expanding $S_\mu$ in a Taylor series to first order in the small parameter $(d'/z_s)$:

$$S_\mu(\eta, z_i) \approx -\frac{\mathrm{j}d'}{\pi z_s}\frac{H_\mu^{(1)}(\eta z_i)}{H_\mu^{(1)}(\eta z_s)}, \quad i = 1, 2. \tag{17}$$

On substituting the Green's functions in (15) into (14), the cross-spectral density is expressed as a triple integral over horizontal wavenumbers $p_1$ and $p_2$, say, and range $r$. The range integral is just the Bessel function closure relation:

$$\int_0^\infty r\,J_0(p_1 r)\,J_0(p_2 r)\,\mathrm{d}r = \frac{\delta(p_1 - p_2)}{p_2}, \tag{18}$$

where $\delta(.)$ is the Dirac delta function, which in this context signifies that components of the noise field with different horizontal wavenumbers are uncorrelated. From the sampling property of the delta function, the remaining two integrals reduce to a single integral, allowing the cross-spectral density to be formulated as

$$\begin{aligned}\langle S_{12}(\omega, z_1, z_2)\rangle &= \frac{\pi\rho\,Q(\omega)\,z'\sqrt{(z_1 z_2)}}{16}\int_0^\infty pS_\mu(\eta, z_1)\,S_\mu^*(\eta, z_2)\,\mathrm{d}p \\ &= \frac{\rho Q(\omega)\sqrt{(z_1 z_2)}\,d'^2}{\pi z_s}\int_0^\infty p\frac{H_\mu^{(1)}(\eta z_1)\,H_\mu^{(1)*}(\eta z_2)}{|H_\mu^{(1)}(\eta z_s)|^2}\,\mathrm{d}p,\end{aligned} \tag{19}$$

where the source depth coordinate, $z'$, has been set equal to $z_s$ outside the integral, and $\eta$ and $\mu$ are as defined in (3) and (4), respectively.

In the absence of volume attenuation in the ocean, the integrand in (19) has an infinite set of second-order poles on the real axis, a consequence of which is that the integral diverges, indicating infinite power in the noise field. This non-physical result, which is somewhat analogous to Olbers' (1826) paradox, arises because the acoustic power at the receivers from each of the sources in the annulus of radius $r$ (figure 2) decays as $r^{-1}$, while the number of sources in the annulus is proportional to $r$, so the total power from the annulus is a constant, independent of $r$. On integrating this constant over an infinite ocean surface, an indefinitely high noise level is obtained.

This difficulty is alleviated by allowing for volume absorption in the ocean, which, in effect, eliminates those acoustic arrivals originating on the sea surface beyond a critical radius determined by the value of the attenuation coefficient at the frequency of interest.

When absorption is taken into account, the second-order poles in the integral in (19) split into two conjugate sets of first-order poles, which fall on either side of the real axis. By integrating around an appropriate contour, as discussed in Appendix A, the cross-spectral density of the noise can be expressed as two branch-line integrals plus an infinite sum of uncoupled normal modes:

$$\langle S_{12}(\omega, z_1, z_2)\rangle = \rho Q(\omega)\sqrt{(z_1 z_2)}\, d'^2/\pi z_s \times\left\{\int_0^{k_\infty} \eta \frac{H^{(1)}_{-j\nu}(\eta z_1) H^{(2)}_{-j\nu}(\eta z_2)}{H^{(1)}_{-j\nu}(\eta z_s) H^{(2)}_{-j\nu}(\eta z_s)}\,\mathrm{d}\eta - \int_0^{\infty} \eta \frac{H^{(2)}_{-j\nu}(\eta z_1) H^{(2)}_{-j\nu}(\eta z_2)}{H^{(2)}_{-j\nu}(\eta z_s) H^{(2)}_{j\nu}(\eta z_s)}\,\mathrm{d}\eta - \frac{e^{2\nu\pi}\pi^2}{8k_\infty \beta z_s^4} \sum_{m=1}^{\infty} \frac{\sigma_m^4}{\sqrt{(\nu^2-\sigma_m^2)}} H^{(1)}_{-j\nu}(j\sigma_m \xi_1) H^{(1)}_{-j\nu}(j\sigma_m \xi_2)\right\}, \tag{20}$$

where $\beta$ is the (frequency dependent) attenuation coefficient of sea water,

$$\xi_i = z_i/z_s, \quad i = 1, 2, \tag{21}$$

are normalized sensor depths, and

$$\nu \equiv j\mu = \sqrt{(k_\infty^2 h^2 - \tfrac{1}{4})}, \tag{22}$$

which is real and positive when the profile supports normal modes. (If $k_\infty h < 0.25$ then $\nu$ is imaginary, in which case there are no poles in the integrand of (19) and hence the normal mode component of (20) is identically zero.)

The eigenvalues, $\sigma_m$, in (20) are solutions of the characteristic equation

$$H^{(1)}_{-j\nu}(j\sigma_m) = 0. \tag{23}$$

As discussed in I, the Hankel function in (23) has an asymptotic form which yields the zeros essentially exactly. They turn out to be the roots of the transcendental equation

$$\nu \ln\left[\frac{\nu + \sqrt{(\nu^2-\sigma_m^2)}}{\sigma_m}\right] - \sqrt{(\nu^2-\sigma_m^2)} - \tfrac{1}{4}\pi = \tfrac{1}{2}(2m-1)\,\pi, \quad m = 1, 2, \ldots. \tag{24}$$

An approximate solution to this equation, obtained by neglecting $\sigma_m$ in both radicals, is

$$\sigma_m \approx 2\nu \exp(\tfrac{1}{4}\pi - m\pi/\nu - 1), \tag{25}$$

which is a satisfactory starting value in a Newton–Raphson iterative routine for finding the 'exact' roots of (24). Computationally, this procedure involves negligible effort, requiring perhaps five iterations to achieve convergence.

The expression in (20) for the cross-spectral density of the noise at two vertically separated sensors in an ocean with an inverse-square profile is exact. It involves the three profile parameters explicitly, as well as the attenuation coefficient $\beta$ in the denominator of the long range, normal mode component. The fact that the depth coordinates of the two sensors, $z_1$ and $z_2$, appear separately in the solution and not as the difference $|z_1 - z_2|$ indicates that in general the inverse-square noise field is spatially inhomogeneous.

A special case of the inverse-square profile is the isovelocity profile, obtained by

setting $h = 0$ in (1). Since all the Hankel functions in (20) are then of order $\frac{1}{2}$ (i.e. $\nu = \frac{1}{2}\mathrm{j}$), they can be expressed exactly in terms of elementary functions, allowing the two integrals in the cross-spectral density function to be evaluated explicitly. The normal mode component, on the other hand, is identically zero because the characteristic equation (equation (23)) has no roots when $\nu$ is imaginary. Thus, the final expression for the isovelocity cross-spectral density consists of just two terms, of which one, associated with the finite integral in (20), is spatially homogeneous, whilst the other, from the infinite integral, is inhomogeneous. The latter is negligible at depths greater than a wavelength below the surface. A comparison of this special case of the inverse-square solution with the known form for the cross-spectral density in an isovelocity ocean (Isakovich & Kur'yanov 1970; Buckingham 1990*a*) shows that the two are identical. A complete account of the cross-spectral density of noise in an isovelocity profile, as derived from the general inverse-square noise theory, is given in Appendix B.

## 4. The cross-spectral density function

In general, the Hankel functions in (20) cannot be expressed in terms of elementary functions, and the integrals and mode sum have to be evaluated numerically. Since the Hankel functions are tedious to compute directly, it is convenient to represent them by their asymptotic forms, which are remarkably accurate.

Taking the eigenfunctions in the mode sum first, it can be shown from Langer's (1932, 1949) turning point theory that Hankel functions of imaginary argument and imaginary order possess the following uniform asymptotic expansion (Balogh 1967; Olver 1974):

$$H^{(1)}_{-\mathrm{j}\nu}(\mathrm{j}\sigma) \approx \mathrm{j}2\sqrt{2}\,\mathrm{e}^{-\nu\pi}(\Omega/(\nu^2-\sigma^2))^{\frac{1}{4}}\,\mathrm{Ai}\,(-\Omega), \tag{26a}$$

where

$$\Omega \equiv \Omega(\sigma) = \left\{\frac{3\nu}{2}\left[\ln\left(\frac{\nu+\sqrt{(\nu^2-\sigma^2)}}{\sigma}\right)-\frac{\sqrt{(\nu^2-\sigma^2)}}{\nu}\right]\right\}^{\frac{2}{3}}, \quad \text{for} \quad \sigma < \nu, \tag{26b}$$

$$\Omega \equiv \Omega(\sigma) = -\left\{\frac{3\nu}{2}\left[\frac{\sqrt{(\sigma^2-\nu^2)}}{\nu}-\arctan\left(\frac{\sqrt{(\sigma^2-\nu^2)}}{\nu}\right)\right]\right\}^{\frac{2}{3}}, \text{ for} \quad \sigma > \nu, \tag{26c}$$

and $\mathrm{Ai}\,(.)$ is the Airy function of the first kind. In I it is shown that an asymptotic form similar to that in (26*a*) is essentially indistinguishable from the original Hankel function for all values of $\nu$ and $\sigma$ relevant to modal propagation.

Hankel functions of imaginary order and real argument, of the type appearing in the integrals in (20), possess a uniform (in the argument) asymptotic expansion of the form (Olver 1954*a*, *b*):

$$H^{(1)}_{\mathrm{j}\nu}(\sigma) \approx -\mathrm{j}\,\mathrm{e}^{\nu\pi/2}\sqrt{(2/\pi)}\,(\nu^2+\sigma^2)^{-\frac{1}{4}}\exp\left[\mathrm{j}\chi(\sigma)\right], \tag{27}$$

where

$$\chi(\sigma) = \sqrt{(\nu^2+\sigma^2)}-\nu\ln\{[\nu+\sqrt{(\nu^2+\sigma^2)}]/\sigma\}+\tfrac{1}{4}\pi. \tag{28}$$

The corresponding asymptotic expansion for the Hankel function of the second kind is obtained by conjugating (27).

On substituting the above uniform asymptotic forms for the Hankel functions into (20), the cross-spectral density of the noise can be expressed as

$$\langle S_{12}(\omega, z_1, z_2)\rangle = (\rho Q(\omega)\sqrt{(z_1 z_2)}\,d'^2/\pi z_s)\{L_1 - L_2 + L_3\}, \tag{29a}$$

where

$$L_1 = \int_0^{k_\infty} \eta \frac{(\eta^2 z_s^2 + \nu^2)^{\frac{1}{2}}}{(\eta^2 z_1^2 + \nu^2)^{\frac{1}{4}} (\eta^2 z_2^2 + \nu^2)^{\frac{1}{4}}} \exp\left[\mathrm{j}\{\chi(\eta z_1) - \chi(\eta z_2)\}\right] \mathrm{d}\eta, \tag{29b}$$

$$L_2 = \int_0^{k_\infty} \eta \frac{(\eta^2 z_s^2 + \nu^2)^{\frac{1}{2}}}{(\eta^2 z_1^2 + \nu^2)^{\frac{1}{4}} (\eta^2 z_2^2 + \nu^2)^{\frac{1}{4}}} \exp\left[\mathrm{j}\{\chi(\eta z_1) + \chi(\eta z_2) - 2\chi(\eta z_s)\}\right] \mathrm{d}\eta, \tag{29c}$$

and

$$L_3 = \frac{\pi^2}{k_\infty \beta z_s^4} \sum_{m=1}^{\infty} \frac{\sigma_m^4}{\sqrt{(\nu^2 - \sigma_m^2)}} \left\{\frac{\Omega(\sigma_m \xi_1)}{\nu^2 - \sigma_m^2 \xi_1^2}\right\}^{\frac{1}{4}} \left\{\frac{\Omega(\sigma_m \xi_2)}{\nu^2 - \sigma_m^2 \xi_2^2}\right\}^{\frac{1}{4}} \times \mathrm{Ai}\left[-\Omega(\sigma_m \xi_1)\right] \mathrm{Ai}\left[-\Omega(\sigma_m \xi_2)\right]. \tag{29d}$$

When $z_1 = z_2$, the expressions in (29) for the cross-spectral reduce to a form which is real and positive, representing the power spectrum of the noise.

Equations (29) represent our final solution for the cross-spectral density of the noise. Each of the three terms in the solution has a different physical interpretation: $L_1$ represents direct path contributions to the noise field, mainly from local, overhead sources; $L_2$ is a near-surface term that is entirely negligible at depths greater than a wavelength beneath the surface; while the mode sum, $L_3$, includes short and long range contributions, arising from sources located all over the sea surface. In general, all three terms exhibit some degree of spatial inhomogeneity. The two integrals, $L_1$ and $L_2$, are complex (except when $z_1 = z_2$), and neither is suitable for evaluation by the method of stationary phase, since the phase functions comprising the arguments of the exponentials show no turning points. The presence of a discrete component, $L_3$, in the noise field is consistent with the modal character of the propagation. Similar discrete terms appear in the expressions for the cross-spectral density of the noise in the Pekeris channel (Buckingham 1980) and the isovelocity, ideal wedge (Buckingham 1985).

The two terms $L_1$ and $L_3$ are not difficult to compute, the integral $L_1$ by a Simpson's rule algorithm and the mode sum, $L_3$, with the aid of a straightforward Airy function routine. By way of contrast, the integral $L_2$ poses some computational problems, associated with the highly oscillatory nature of the integrand and the upper limit of infinity on the integral. However, an order of magnitude estimate for $L_2$ may be derived on the assumption that the major contribution to the integral arises from the region where $\eta z_s \gg \nu$. The integral may then be written in the form (see Appendix B)

$$\begin{aligned} L_2 &\approx \frac{z_s}{\sqrt{(z_1 z_2)}} \int_0^{\infty} \eta \exp(-\mathrm{j}a\eta)\, \mathrm{d}\eta \\ &= \mathrm{j} \frac{z_s}{\sqrt{(z_1 z_2)}} \frac{\mathrm{d}}{\mathrm{d}a} \int_0^{\infty} \exp(-\mathrm{j}a\eta)\, \mathrm{d}\eta \\ &= \mathrm{j} \frac{z_s}{\sqrt{(z_1 z_2)}} \frac{\mathrm{d}}{\mathrm{d}a} \left[\pi\delta(a) - \frac{\mathrm{j}}{a}\right], \end{aligned} \tag{30a}$$

where

$$a = (z_1 + z_2 - 2z_s) \tag{30b}$$

is twice the mean depth (beneath the surface) of the sensors. On taking the derivative in (31*a*), and recognizing that the delta function may be neglected since it is zero when either sensor lie below the surface, the final result for $L_2$ is found to be

$$L_2 \approx -z_s / \{\sqrt{(z_1 z_2)}\, (z_1 + z_2 - 2z_s)^2\}. \tag{31}$$

As with the inhomogeneous component of the noise field in isovelocity water (Appendix B), the dimensionless quantity $L_2/k_\infty^2$ is inversely proportional to the square of ($k_\infty$ times the mean depth of the sensors), indicating that at depths of more than one wavelength below the surface, $L_2$ makes a negligible contribution to the noise.

## 5. Ambient noise in the Greenland Sea: inverse-square theory

For several years, the Defence Research Agency, Farnborough, United Kingdom (previously, the Royal Aerospace Establishment) has been conducting a programme of airborne ocean-acoustics research in the marginal ice zone (MIZ) off the east coast of Greenland between the Denmark Strait ($\approx 68°$ N, 25° W) and the Fram Strait ($\approx 80°$ N, 0° W) (Buckingham 1990*b*). As part of the programme, measurements of the omni-directional ambient noise and the temperature profile have been made in the MIZ. The measurements are obtained by dropping calibrated sonobuoys and aircraft-expendable-bathythermographs (AXBTs) from a fixed-wing aircraft (a BAC 1-11 twin-engine jet) into leads of open water between ice floes.

Acoustic data are collected with two different types of buoy, covering overlapping frequency bands, designated very-low-frequency (VLF), extending from 5 Hz up to 200 Hz, and low-frequency (LF), from 50 Hz up to 5 kHz. The VLF buoys are specially designed with flow-shielding and other features to alleviate self-noise problems below 50 Hz (Strasberg 1979). As standard practice, we co-locate one VLF and one LF buoy at each measurement position. Measurements have been made in all seasons and in weather conditions ranging from sea-state zero (0) to sea-state six (6). (At higher sea states the buoys experience washover, which degrades the radio frequency telemetry transmissions by inducing data dropout.)

Before discussing one set of noise spectra (§6), observed in summer 1988, we evaluate the inverse-square theory and examine its predictions in connection with the noise field in the experimental area. To begin, values are assigned to the three inverse-square profile parameters, based on the requirement that (1) should show a reasonable fit to a sound speed profile that is representative of the ocean-acoustic conditions in the observation area.

### (*a*) *The summer sound speed profile*

Although AXBTs are dropped from the research aircraft, giving a spot temperature profile, no salinity profile is taken at the time the acoustic measurements are made. Since the presence of the partial ice cover tends to reduce the near-surface salinity, it is necessary to assume some appropriate form for the variation of salinity with depths in order to estimate the sound speed profile.

Johannessen *et al.* (1986) made hourly conductivity-temperature-depth (CTD) observations in the Fram Strait on 3 and 4 July 1983, when weather conditions were calm (winds less than 5 m s$^{-1}$). Their averaged salinity profile, from 48 CTD casts, shows only a mild variation with depth, increasing approximately linearly from a surface value of 34 parts per thousand (‰) to 35‰ at a depth of 150 m, remaining essentially constant thereafter. (A salinity increment of 1‰ corresponds to a sound speed increase of approximately 1 m s$^{-1}$). Their averaged temperature profile is very similar to our AXBT data taken at the time of the noise measurements, but extends 200 m deeper into the ocean. The sound speed profile depicted by the crosses in figure 3 was calculated from the averaged temperature and salinity data of Johannessen *et*

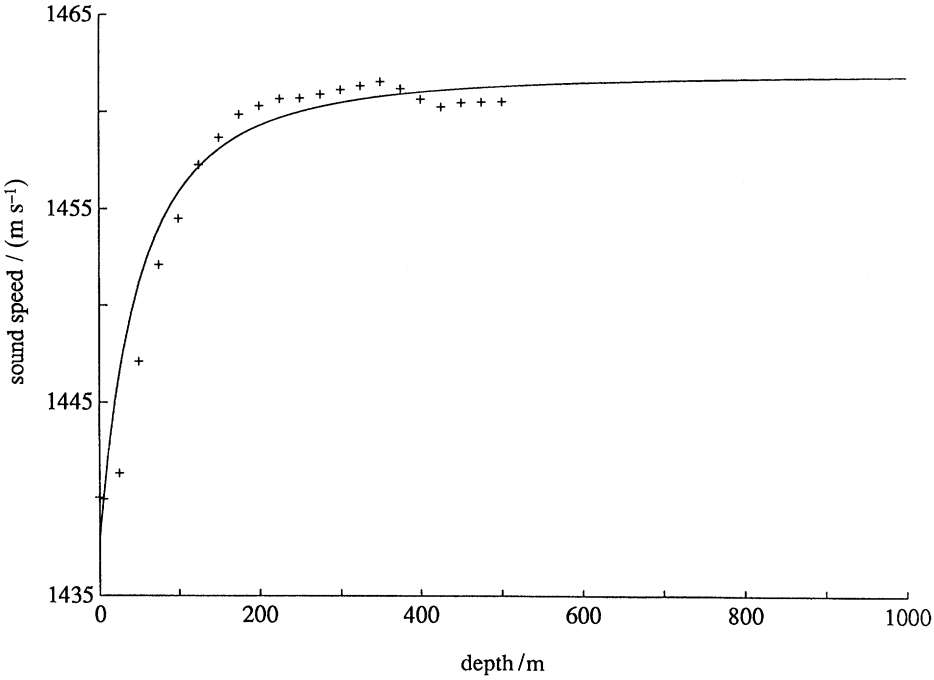


Figure 3. Sound speed profile (crosses) derived from averaged CTD data (see text for details). The solid line is an inverse-square profile with parameters $h = 18.34$ m, $z_s = 100$ m, and $c_\infty = 1462$ m s$^{-1}$.

*al.* (1986) using an empirical polynomial expression due to Mackenzie (1981*a*, *b*). This profile is very similar to many of those reported by Meredith *et al.* (1989), as illustrated for example by their CTD Cast 19B, and is considered to be a good representation of the summer sound speed conditions that pertained when our ambient noise measurements in the Greenland Sea were made.

The inverse-square profile can be fitted reasonably well to the sound speed data of Johannessen *et al.* (1986), as illustrated by the solid line in figure 3. The values of the inverse-square parameters used to achieve the fit are: $h = 18.34$ m, $z_s = 100$ m, and $c_\infty = 1462$ m s$^{-1}$, corresponding to a surface sound speed of 1438 m s$^{-1}$. These profile parameters are used hereafter in the inverse-square noise theory to interpret the spectral and spatial characteristics of summer-time ambient noise in the Fram Strait.

### (*b*) *The attenuation coefficient*

The absorption coefficient, $\beta$, which appears as a factor in the mode sum, $L_3$, must also be specified in order to evaluate the inverse-square noise theory. For frequencies below 10 kHz, Kibblewhite & Hampton (1980) have proposed the following form for the attenuation coefficient, $\alpha$, expressed in dB km$^{-1}$:

$$\alpha = \alpha_s + 0.11Kf^2\{1+(f/f_0)^2\}^{-1} + 0.011f^2, \tag{32}$$

where $f$ is frequency in Hertz and $\alpha_s$ is a frequency-independent term, of uncertain physical origin but possibly associated with scattering from turbulence, which is dominant at frequencies below 100 Hz. Equation (32) is a modification of the form for $\alpha$ originally proposed by Thorp (1965, 1967). The value of $\alpha_s$ depends on the nature of the water mass, showing regional variations within the range $2\times10^{-4}$–$4.2\times10^{-3}$ dB km$^{-1}$. The second term on the right of (32) represents

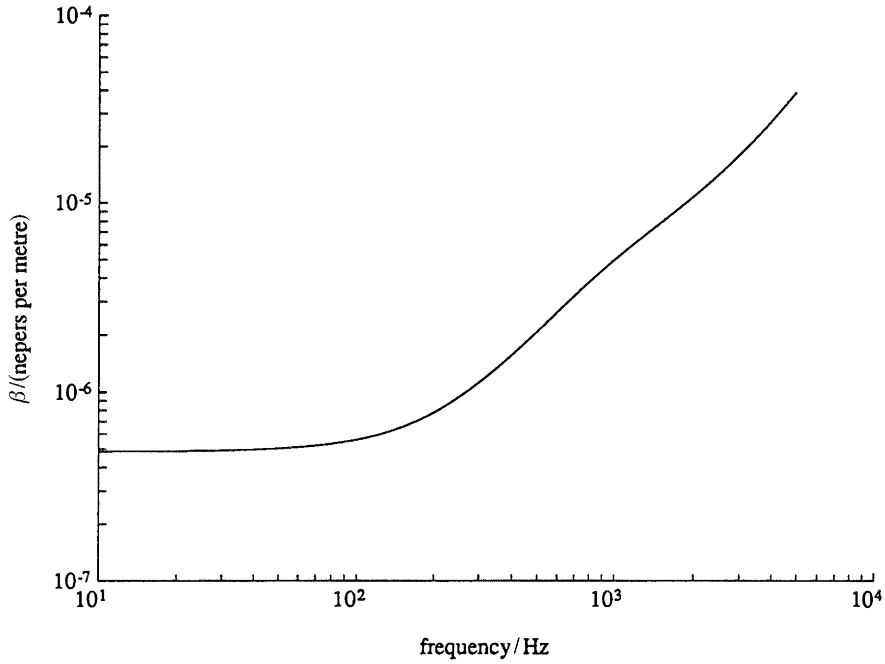


Figure 4. The absorption coefficient, $\beta$, as a function of frequency.

absorption due to the relaxation of boric acid, whose relaxation frequency is $f_0 =$ 1 kHz; and the third term is associated with the relaxation of magnesium sulphate, whose relaxation frequency is around 65 kHz. The factor $K$ in the boric acid term is a pH-dependent parameter whose value lies between 0.5 and 1.1. Kibblewhite & Hampton (1980) suggest that appropriate values of $\alpha_s$ and $K$ for polar waters are $4.2 \times 10^{-3}$ dB km$^{-1}$ and 0.5, respectively; and accordingly, these values are adopted below in our evaluation of the inverse-square noise theory.

In passing, it is worth remarking that the existence of an excess attenuation at frequencies below 100 Hz, as represented by $\alpha_s$ in (32), has on occasion been called into question. The reason for the doubts about its reality is the assumption of cylindrical spreading that is conventionally adopted in interpreting long range, VLF propagation data. To avoid this difficulty, Kibblewhite *et al.* (1976) conducted a novel experiment in which relative levels of VLF ambient noise were compared at two sites about 1000 km apart in the North Pacific. This differential noise measurement yielded a value for $\alpha_s$ that is consistent with the values derived by more conventional propagation techniques, but which did not rely on the assumption of cylindrical spreading. From this and other evidence, the existence and magnitude of the VLF excess attenuation is now fairly well accepted.

In the inverse-square expression for the cross-spectral density of the noise, the attenuation coefficient, $\beta$, is in nepers per metre. Thus $\beta$ is related to $\alpha$ through the scaling law

$$\beta = \alpha/2 \times 10^4 \times \log(e). \tag{33}$$

Figure 4 shows $\beta$ plotted as a function of frequency, as evaluated from (32) and (33).

### (*c*) *An empirical source strength function*

The magnitude of the expression for the cross-spectral density in (29*a*) depends on several source parameters: the rate of events per unit area of surface, $\rho$, the depth of the noise sources, $d'$, and the magnitude of the source strength function $Q(\omega)$. No attempt is made here to derive theoretical estimates of these parameters, since our emphasis is on propagation phenomena rather than source mechanisms but we shall assume that the frequency dependence of $Q(\omega)$ is given by a power law of the form

$$Q(\omega) \propto f^{-3.2}. \tag{34}$$

(The source strength function, $Q(\omega)$, is distinct from the 'surface noise source level' (Burgess & Kewley 1983) and the 'source level density' (Wilson 1983), both of which relate to the level and spectral shape of the ambient noise field as observed at some point in the ocean. These terms do not relate explicitly to the spectral shape of the sources.) As discussed later, when the empirical relationship in (34) is used in the inverse-square theory, it provides a good match to one particular set of noise spectra that we acquired in the vicinity of the ice edge near the Fram Strait.

### (*d*) *The* MIZ *power spectrum*

Figure 5 shows the power spectrum calculated from the inverse-square theory using the parameter values derived above. In evaluating the theoretical spectrum, the depth of the sensor has been taken as 160 m, corresponding to the depth setting of the hydrophones used in our ambient noise measurements. For convenience in making comparisons with the experimental data, the VLF (5 to 200 Hz) and LF (50 Hz to 2 kHz) spectral regimes are considered separately.

Taking the VLF spectrum first (figure 5*a*), the near-surface term, $L_2$, is seen to be negligible at all frequencies above 5 Hz (that is, over the whole frequency range of the data). At frequencies above 20 Hz the modal component $L_3$ dominates the direct path term $L_1$; but below 20 Hz the modes are no longer supported by the profile and $L_3$ drops dramatically. As the direct path term shows a fairly steep negative slope in this region, the net effect is a minimum in the spectrum at about 10 Hz. The slow oscillations present in the VLF spectrum can be identified with individual modes in $L_3$. The minimum at 10 Hz is significant, since a similar feature appears in the measured ambient noise spectra from the Greenland Sea.

Turning to the low frequency curves in figure 5*b*, it is evident that over the whole frequency range the direct path term $L_1$ shows a uniform (logarithmic) slope of $-1.3$ ($-13$ dB per decade). Between 50 and 100 Hz, where the attenuation coefficient is essentially independent of frequency, the mode sum, $L_3$, shows a (logarithmic) slope close to $-1.5$ ($-15$ dB per decade); but at higher frequencies the attenuation coefficient varies as the square of the frequency, as a result of which $L_3$ decays more rapidly, eventually dropping below the near-field term, $L_1$, at about 500 Hz. Thus, the low-frequency spectrum is almost entirely modal at frequencies below 100 Hz or so, then passes through a transition region of somewhat steeper (negative) slope, to become almost entirely direct path at 2 kHz and above. The kink in the spectrum centred on a frequency of about 400 Hz and associated with the transition from modal to near-field noise will be important later in interpreting low-frequency spectra observed in the Greenland Sea. Incidentally, the presence of the kink in the noise data is supporting evidence for the existence of the frequency independent, excess attenuation term, $\alpha_s$, in the expression for the attenuation coefficient in (32).

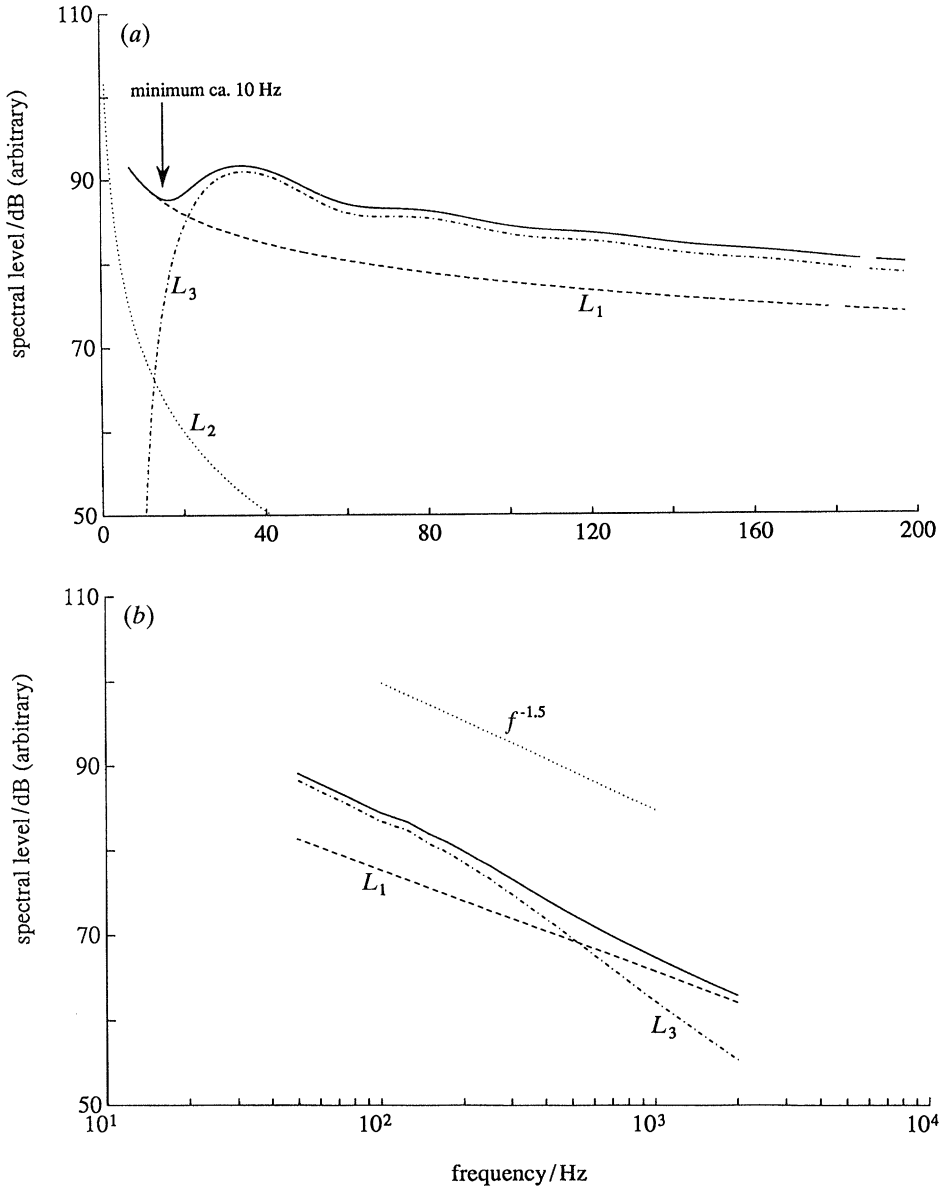


Figure 5. Spectra for the MIZ from the inverse-square theory, for a receiver 160 m below the surface. (*a*) Very-low-frequency (5 to 200 Hz) on log-linear scales. (*b*) Low-frequency (50 Hz to 2 kHz) on log–log scales. The dashed and dash–dot lines represent the contributions from the integral $L_1$ and the mode sum $L_3$, respectively; the dotted curve in (*a*) is the contribution of the near-surface term, $L_2$ and the solid line in (*a*) and (*b*) is the total spectrum. For reference, the straight dotted line in (*b*) shows a logarithmic slope of $-1.5$ (i.e. $-15$ dB per decade). $L_2$ is not shown in the LF spectrum since it is entirely negligible.

Figure 6 shows the inverse-square power spectrum at four frequencies, 20, 100, 500 and 1000 Hz, as a function of depth (beneath the surface). In all cases, the noise level below 2 km is small compared with the levels at depths of a few hundred metres. An important implication of this result is that, when the sea floor is at a depth of 2 km or more, the effect of acoustic bottom interactions must be negligible on the near-




PHILOSOPHICAL TRANSACTIONS OF THE ROYAL SOCIETY A MATHEMATICAL, PHYSICAL & ENGINEERING SCIENCES

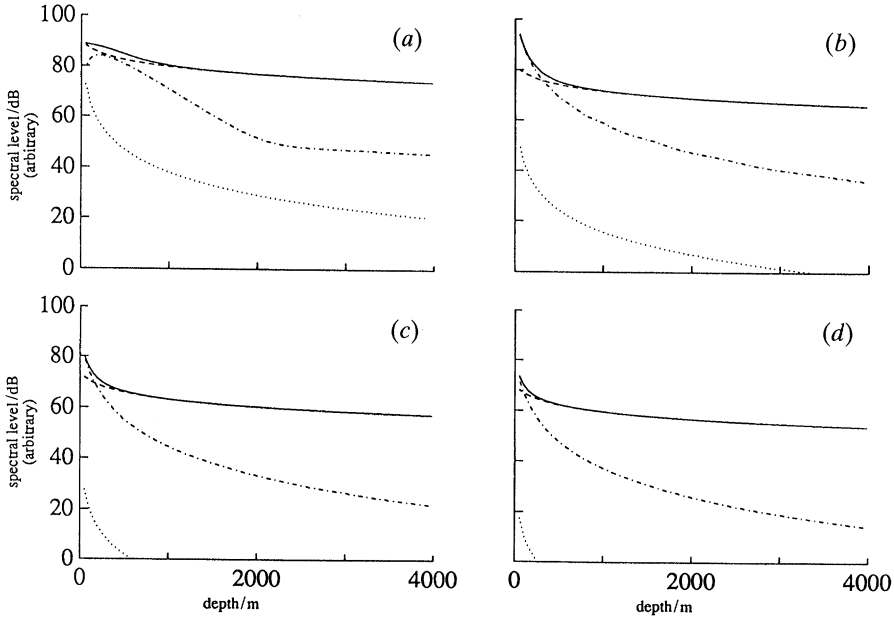


Figure 6. MIZ noise spectra as a function of depth for four frequencies, from inverse-square theory. The dashed line is the direct path component, $L_1$, the dotted line is the near-surface component, $L_2$, the dash–dot line is the modal component, $L_3$ and the solid line is the total spectrum. $f = 20$ Hz (*a*), 100 Hz (*b*), 500 Hz (*c*), 1 kHz (*d*).

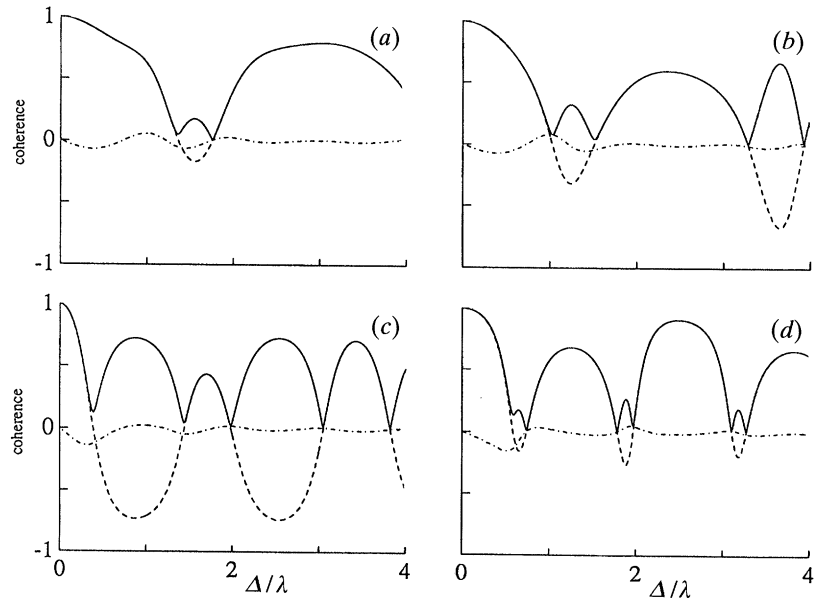


Figure 7. Coherence plots from the MIZ inverse-square theory for a frequency of 100 Hz. The solid, dashed and dot–dash curves are the magnitude, real part and imaginary part, respectively, of the coherence function. ($L_2$ was neglected in computing these curves.) Mean depth = 100 m (*a*), 200 m (*b*), 500 m (*c*), 1000 m (*d*).

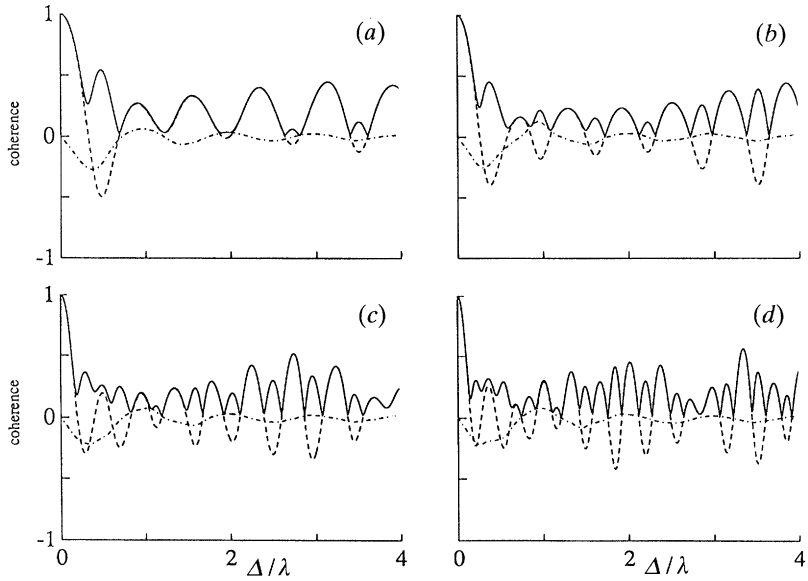


Figure 8. Coherence plots from the MIZ inverse-square theory for a frequency of 500 Hz. The solid, dashed and dot–dash curves are the magnitude, real part and imaginary part, respectively, of the coherence function. ($L_2$ was neglected in computing these curves.) Mean depth = 100 m (*a*), 200 m (*b*), 500 m (*c*), 1000 m (*d*).

surface noise field. This is true even at 20 Hz, where the noise level at a depth of 2 km is 12 dB or so less than that at 100 m.

### (*e*) *Vertical spatial coherence*

The expressions for the cross-spectral density in (29) can be used in (13) to give the vertical spatial coherence of the noise. By treating the mean depth of the two sensors as a parameter, the spatial coherence can be conveniently examined as a function of the sensor separation, the usual convention being to express the latter in terms of wavelengths. Variations in the coherence function with the mean depth of the sensors indicate the degree of spatial inhomogeneity exhibited by the noise field.

Examples of the coherence function for our Greenland Sea parameters are shown in figures 7 and 8 for frequencies of 100 Hz and 500 Hz, respectively. On the abscissae, $\Delta = (z_2 - z_1)$ is the sensor separation and $\lambda$ is the acoustic wavelength. At both frequencies the noise coherence shows a strong dependence on the mean depth of the sensors, even below 500 m, where the sound speed profile is essentially uniform. One implication of these curves is that a vertical array of even modest aperture, say 100 m, placed anywhere in the water column, would be exposed to a noise field whose coherence (i.e. directional) properties differ substantially from top to bottom. Plane-wave beamforming in these circumstances, aimed at determining the 'directionality' of the noise, would be inappropriate since no unique directional density function exists.

The profound effect of the inverse-square profile on the noise field is evident in figures 7 and 8, not only through the variations with mean depth, but also through the frequency dependence of the coherence function. This makes an interesting comparison with surface-generated noise in an isovelocity ocean, which is spatially homogeneous at depths greater than a wavelength and shows a coherence function

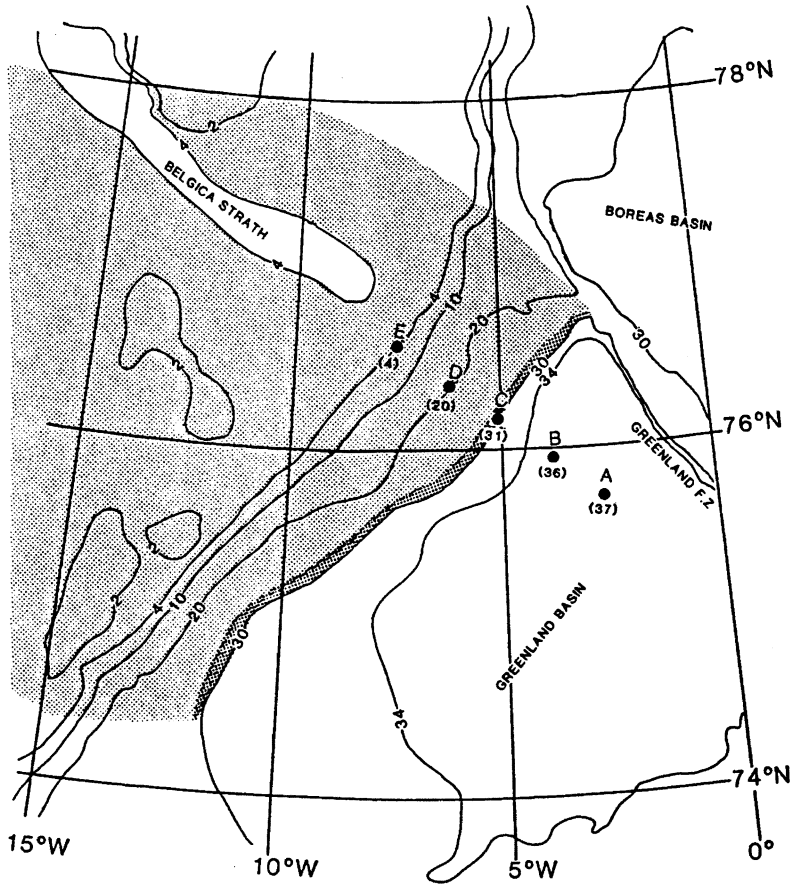


Figure 9. The bathymetry, ice cover (shading) and sonobuoy configuration (collinear positions A to E) in DRA ambient noise ice-edge experiment. The numbers on the depth contours and the bracketed numbers by the buoy positions denote depth in hundreds of metres. Sites A and E at either end of the track are at positions 75° 44′ N, 03° 03′ W and 76° 37.6′ N, 07° 32.2′ W, respectively, corresponding to a nominal separation between nearest-neighbour buoy pairs of 36 km. The high concentration of floes at the ice edge, which runs along the 3000 m contour, is depicted by the ribbon of darker shading.

that depends only on the ratio $\Delta/\lambda$ (Appendix B, equation (B 6)). Thus, under isovelocity conditions, coherence plots like those in figures 7 and 8 would show all eight panels as identical.

## 6. Ambient noise in the Greenland Sea: experiment

On 4 August 1988, as part of the programme of Arctic airborne acoustic research in the MIZ described in the preceding section, five pairs of omni-directional sonobuoys (one VLF and one LF buoy in each pair) were dropped in a line perpendicular to the ice edge in the vicinity of the Fram Strait. Figure 9 shows the positions of the buoy pairs, labelled A (easternmost) to E (westernmost), with C being the position at the ice edge itself. The separation between adjacent buoy pairs was nominally 36 km, and all hydrophones were at a nominal depth of 160 m. It can be seen from the depth contours in figure 9 that at the four positions A to D the water is deep, 2000 m or

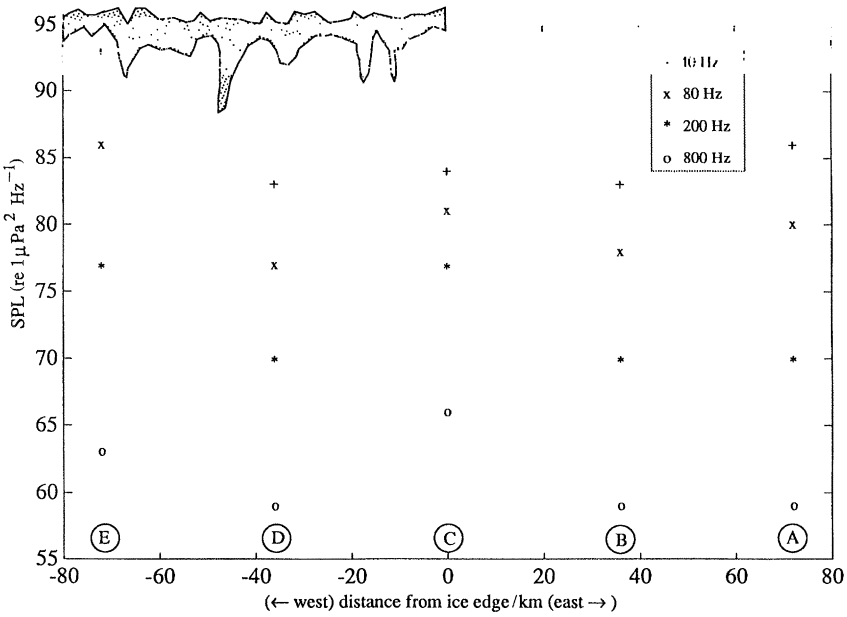


Figure 10. Spectral levels along the track perpendicular to the ice edge. Note the reduced peak at the ice edge at 40 Hz.

greater, but that the fifth position, E, is over the Greenland continental shelf, where the depth is less than 400 m. (For the detailed bathymetry of the region see Perry (1986).) Effects of the shallow water at site E can be seen in the VLF and LF noise spectra described below.

In the open ocean, the sea state was 1 to 2 with no visible swell. A few kilometres west of the ice edge, which was fairly compact, the ice concentration was about 6/10, but near the ice edge itself the concentration was considerably higher (figure 9), presumably as a result of an earlier on-ice wind. At the time of the experiment a light breeze (wind speed of 3.5 m $s^{-1}$) was blowing out of the northeast (i.e. roughly parallel to the ice edge). The ice floes were relatively small at the ice edge, of the order of metres in diameter, but deeper into the ice cover the floe diameters increased to tens of metres at position D, 36 km from the ice edge, and hundreds of metres at position E, 72 km from the edge.

### (*a*) *Spatial variation of the noise across the ice edge*

Figure 10 shows the sound pressure levels observed at four frequencies, 40, 80, 200 and 800 Hz at each of the five buoy locations. At the ice edge the spectral level shows a maximum at all four frequencies, although at the two lower frequencies the peak is less pronounced, especially so at 40 Hz, where the level at the ice edge is little different from that at the adjacent buoys 36 km either side of the edge. The presence of the ice-edge peak in figure 10 is consistent with the observations of Diachok & Winokur (1974), who reported noise measurements across the edge at 100, 315 and 1000 Hz. They suggest that the ice edge acts as a strong broadband line source.

Perhaps a more descriptive term is 'ribbon source', since the acoustically active region is a strip several kilometres wide extending along the ice edge. Qualitatively at least, the high level of sound at the ice edge is consistent with the fact that, due to the action of waves and swell (Wadhams 1986), the edge is a very energetic region, where floe–floe interactions (bumping, grinding, etc.) are frequent and violent. It is

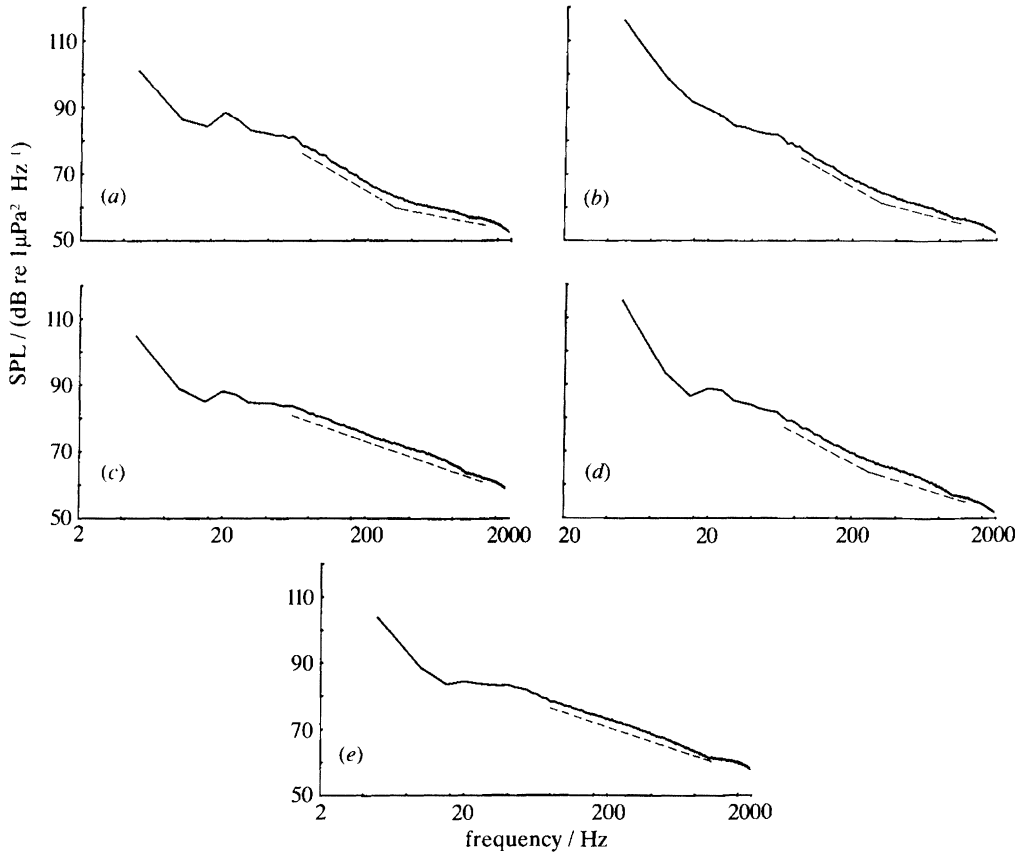


Figure 11. Averaged LF spectra observed at sites A to E across the ice edge. In (*a*), (*b*) and (*d*), the two broken lines indicate the kink in the spectra at about 400 Hz. The single broken line in (*c*) and (*e*) illustrates the uniform slope of the spectra. (*a*) Position A (open ocean, water depth 3700 m); (*b*) position B (open ocean, water depth 3600 m); (*c*) position C (ice edge, water depth 3100 m); (*d*) position D (ice cover, water depth 2000 m); (*e*) position E (ice cover, water depth $< 400$ m).

reasonable to expect that such interactions would be very noisy. Our observation at the time of the experiment – that the floes were small in the vicinity of the edge but increased in size dramatically with distance into the ice cover – supports the view that most of the wave–ice interaction had indeed occurred within several kilometres of the ice edge.

The reduced level (figure 10) of the ice-edge peak at the lower frequencies can be interpreted in terms of the principal spectral components of the noise predicted by the inverse-square theory (figure 5). Suppose that the surface sources are made up of two distributions: a background of sources uniformly distributed (statistically) across the whole sea surface, upon which is superimposed the highly energetic ribbon of sources associated with the ice edge (figure 9). As far as the buoy at the ice edge is concerned, the direct path component of the noise field ($L_1$) originates in local, overhead sources, that is to say primarily from within the high-energy ribbon. The normal mode component ($L_3$), on the other hand, is driven mainly by the distant background sources (since the number of distant sources in the narrow, energetic ribbon is relatively small). Accordingly, $L_3$ should show much the same level as if the ice-edge sources were absent, whereas $L_1$ should be enhanced by their presence. Thus,

at the ice edge buoy, we expect $L_1$ to be higher relative to $L_3$ than is indicated in figure 5*b*, which shows the relative levels when both components originate in a uniform distribution of surface sources.

To investigate the implications of this shift in relative magnitudes arising from the ice-edge ribbon, suppose that $L_1$ in figure 5*b* were raised by a nominal 8 dB. At frequencies of 100 Hz and above, $L_1$ then becomes the dominant component in the noise spectrum, leading to an enhancement of 8 dB or so in the total spectral level. This is representative of the situation at the ice edge and, since $L_1$ is a local phenomenon, is consistent with the observation of the ice-edge peak (figure 10). At lower frequencies, however, because of the steeper slope of $L_3$, the enhanced $L_1$ is not predominant but only comparable to or somewhat less than $L_3$. In this case the total noise level at the ice edge should be much the same as at other locations along the line of buoys, again in accord with the observations. We conclude that the frequency dependence exhibited by the ice edge peak in figure 10 arises directly from the spatially non-uniform distribution of energetic sources aligned along the ice edge. These sources enhance the direct path but not the modal component of the noise at the higher frequencies.

A second interesting feature of figure 10 is the relatively high spectral levels observed at all frequencies at the westernmost pair of buoys (location E), nearest the Greenland coast. Whatever the origin of these high levels, the generating mechanism is almost certainly a localized process, since the phenomenon is observed at only one location. A plausible hypothesis is that the locally enhanced levels are due to increased source levels associated with the very large floes in the region, driven perhaps by wind rather than surface waves, which are heavily attenuated so far into the ice cover. The fact that these energetic sources do not affect the buoys at the other locations may be due to mode stripping arising from the proximity of the bottom. Some support for this argument is presented in the following discussions of the LF and VLF spectra observed at site E.

### (*b*) *Low-frequency spectra*

The LF spectra obtained from the five locations along the track perpendicular to the ice edge are shown in figure 11. Each spectrum is an average of 1000 individual spectra taken over an interval of 200 s, giving a spectral resolution of 5 Hz. As with the spatial plot in figure 10, the features on the five spectra can be interpreted in terms of the inverse-square noise theory developed in §5.

The spectra from the two LF buoys at positions A and B in the open ocean, where the water depth is *ca.* 3700 m and bottom interactions are negligible, are shown in figure 11*a*, *b*. Both spectra show a change of (logarithmic) slope at about 400 Hz. This behaviour is in accord with the theoretical spectrum in figure 5*b*, leading to the conclusion that the spectra are dominated by the modal component ($L_3$) below 400 Hz and the direct path component ($L_1$) at higher frequencies.

The spectrum from the LF buoy at position C on the ice edge does not show a kink but has a uniform slope from 80 Hz to 1 kHz (figure 11*c*), suggesting that the direct path component is dominant over this frequency band. This is consistent with our interpretation of the ice-edge peak in figure 10: most of the noise originates in the high-energy, overhead sources at the ice edge, with the distant background sources making a small contribution by comparison. No mode stripping is possible through bottom interactions (figure 6) because the water depth (*ca.* 3100 m) is too great.

A change in slope at few hundred hertz reappears in the spectrum from the LF buoy

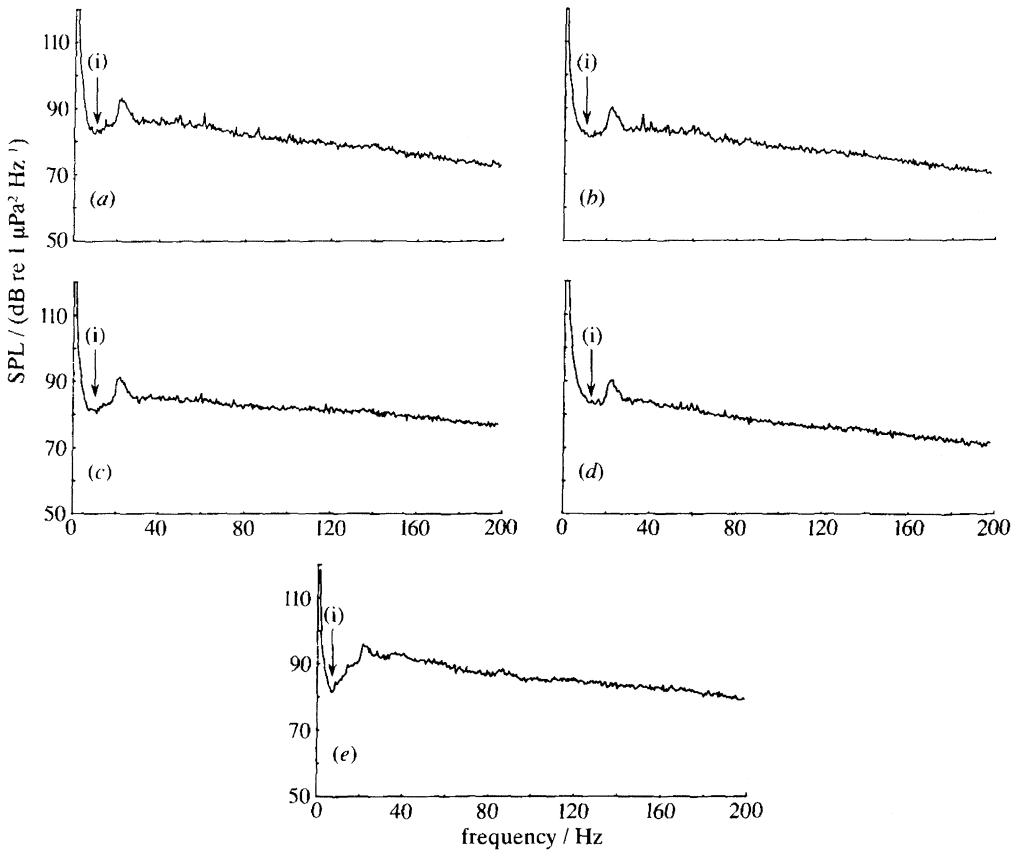


Figure 12. Averaged VLF spectra observed at sites A to E, as detailed in figure 11, across the ice edge. (i) Minimum *ca.* 10 Hz.

at position D, 36 km into the ice (figure 11*d*). Bottom interactions are negligible (figure 6), since the water depth is 2000 m; and the interpretation of the spectrum is the same as with the spectra at positions A and B.

The spectrum from the last LF buoy in the line, at position E, where the water is only 400 m deep, does not show a change of slope around 400 Hz (figure 11*e*). This is consistent with the hypothesis in §6*a* that bottom interactions reduce significantly the modal component of the noise, the effect being to leave the direct path, uniform slope component as the principal contributor to the spectrum above 100 Hz. The enhanced LH spectral levels at this position, shown in figure 10, could possibly be attributed to the massive ice floes that are present so deep in the ice cover, which, driven by wind, act as very energetic sources.

### (*c*) *Very-low-frequency spectra*

The spectra from the VLF buoys at positions A to E are shown in figure 12. Each spectrum is an average of 100 individual spectra taken over an interval of 200 s, giving a spectral resolution of 0.5 Hz. Two prominent features at all locations are a peak just above 20 Hz and a minimum centred around 10 Hz. Below 5 Hz, where it is known that the effectiveness of the flow shielding is reduced, the high noise level is probably not a genuine acoustic signal but an artefact associated with hydrodynamic flow around the hydrophone.

The origin of the 20 Hz peak is uncertain but it may be produced by marine mammals, notably the finback whale (Watkins *et al.* 1987), although there are some difficulties with the finback hypothesis. An alternative possibility is that the peak originates in some coastal process, one candidate being slumping glaciers descending 2000 m or so over bedrock from the Greenland ice cap to sea level. Both the finback whale and slumping-glacier hypotheses are discussed by Buckingham (1990*b*).

In the present context, the more important feature in the spectra of figure 12 is the minimum at 10 Hz. It corresponds accurately to the minimum predicted by the inverse-square theory (figure 5*a*) and is interpreted accordingly: below 20 Hz, the modal component ($L_3$) of the noise shows a steep positive slope, associated with mode drop-out, whereas the direct path component ($L_1$) shows a negative slope, the cross-over between the two falling at about 10 Hz, giving rise to the observed minimum. The 10 Hz minimum is a ubiquitous feature of our noise spectra from the MIZ, appearing in all weather conditions and seasons of the year.

At the deep, open ocean positions A and B, the VLF spectra are consistent with the theoretical form in figure 5*a*. Accordingly, they are interpreted as consisting of a combination of direct path and normal mode components, arising from a uniform distribution of surface sources. The noise level at the ice edge, position C, is several dB higher above 100 Hz than the levels at A and B. As with the ice-edge peak in the spatial distribution in figure 10, this is interpreted as arising from a relative increase in the direct path component, associated with the localized distribution of sources at the edge, as described in §6*a*. Below 100 Hz at position C, the normal mode component takes over as the major contributor to the noise, its presence being evident from the rapid roll-off below 20 Hz.

The VLF spectrum at position D is consistent with a uniform distribution of surface sources, much like the spectra at A and B, and can be interpreted according to the inverse-square curves in figure 5*a*. At site E, deep into the ice cover, the VLF levels show a noticeable enhancement, perhaps due to large floes acting as energetic acoustic sources. The normal mode component shows a roll-off below 20 Hz that is more rapid than at the other locations, behaviour that could reasonably be attributed to excess mode attenuation through bottom interactions, since the water is shallow at this position.

### (*d*) *Noise data versus the inverse-square theory: summary*

On the whole, the spatial distribution and frequency dependence of the noise data that were taken across the ice edge are consistent with the inverse-square noise theory, provided the high concentration of intensive surface sources at the ice edge itself is taken into account. It is also necessary to postulate an energetic source distribution deep into the ice cover to accommodate the high noise levels observed there. Minor discrepancies between the theory and observations could possibly be explained by fine structure in the spectral shape of the sources, which has not been incorporated into the theory. The important point, however, is that, except for the frequency dependence of the source strength specified in (34), most of the major features of the VLF and LF ambient noise spectra observed across the ice edge are effects of the upward refracting propagation conditions.




PHILOSOPHICAL TRANSACTIONS OF THE ROYAL SOCIETY A MATHEMATICAL, PHYSICAL & ENGINEERING SCIENCES

## 7. Concluding remarks

Ambient noise in the ocean is an interesting, complicated phenomenon, whose spatial and spectral properties depend on the nature of the sources and the acoustic propagation conditions prevailing beneath the surface. Since acoustic signal detection in the ocean is performed against the noise background, the noise has traditionally been regarded as a nuisance, being the factor that degrades the signal-to-noise ratio. Although this is an understandable point of view, it overlooks the fact that the structure of the noise field is characterized by the ocean environment. Thus, the noise contains information about oceanic processes and properties, including, for example, the geo-acoustic structure of the bottom and rates of gas transfer across the air–sea interface. In principle, this information can be extracted from the noise, offering the prospect of conducting acoustical oceanography without the need for man-made sound sources.

To make full use of the noise, the propagation conditions in the medium must be taken into account. Most existing theories of ambient noise assume an isovelocity ocean, which for shallow, well mixed channels may be reasonable but more generally is not valid. Unfortunately, the mathematics of acoustic propagation in most non-isovelocity profiles rapidly becomes intractable, rendering a noise analysis impossible. The inverse-square profile for a semi-infinite ocean (equation (1)) is an exception in that exact analytical expressions can be developed for the propagation (the Green's function) and for the vertical coherence of the ambient noise.

As the inverse-square profile is monotonic increasing with depth, it represents a relatively simple oceanic sound speed profile, of the type that is found in the polar oceans, the surface sound channel and the ocean-surface bubble layer. For these environments, the inverse-square noise theory provides a useful tool for interpreting noise coherence data, as well as providing the basis of inverse techniques for extracting oceanographic information from the natural sound field in the ocean.

The acoustic data from the marginal ice zone were acquired by the Royal Aerospace Establishment, Farnborough, United Kingdom (now the Defence Research Agency, Farnborough, U.K.), using their fixed-wing research aircraft and their scientific support staff. I am indebted to the DRA for supporting the Arctic experimental programme and for making the data available. Peter Martinson and Julian Fletcher of the DRA have been central to the programme from its inception. The skill and cooperation of the aircrews of the Experimental Flying Department, DRA, Farnborough is appreciated. Support for the research was also received from the United States Office of Naval Research under contract N00014-91-J-1118.

## Appendix A. The integral for the cross-spectral density

From (19), the expression for the cross-spectral density of ambient noise in an ocean supporting an inverse-square profile is

$$\langle S_{12}(\omega, z_1, z_2)\rangle = \frac{\rho Q(\omega)\sqrt{(z_1 z_2)}\,\mathrm{d}'^2}{\pi z_s}\int_0^\infty p\,\frac{H_\mu^{(1)}(\eta z_1)\,H_\mu^{(1)*}(\eta z_2)}{|H_\mu^{(1)}(\eta z_s)|^2}\,\mathrm{d}p. \tag{A 1}$$

Although this expression is generally valid, it is inconvenient to evaluate numerically because of poles in the integrand which are on or very close to the path of integration, to say nothing of the difficulty of computing Hankel functions of imaginary argument and order. To convert the integral to a more tractable form, we turn to contour integration in the complex $p$-plane.

The integral in question is

$$I_{12} = \int_0^\infty p \frac{H_\mu^{(1)}(\eta z_1) H_\mu^{(1)*}(\eta z_2)}{H_\mu^{(1)}(\eta z_s) H_\mu^{(1)*}(\eta z_s)} \mathrm{d}p, \tag{A 2}$$

where

$$\eta = \sqrt{(k_\infty^2 - p^2)} = |k_\infty^2 - p^2|^{\frac{1}{2}} \mathrm{e}^{\mathrm{j}\theta}. \tag{A 3}$$

The radical, $\eta$, has branch points at $p = \pm k_\infty$; and the values of the phase angle, $\theta$, throughout the $p$-plane will depend on our choice of branch cuts.

Before addressing the question of branch cuts, however, a more fundamental problem must be considered: since conjugated terms are present, is the integrand an analytic function of $p$? We argue that it is, or at least can be treated as such, provided the process of conjugation is handled appropriately. The conjugated Hankel functions in (A 2) can be expressed in the form

$$[H_\mu^{(1)}(x)]^* = H_{\mu^*}^{(2)}(x^*), \tag{A 4}$$

indicating that, instead of $\eta$, the variable to consider in the argument of these functions is

$$\zeta = [\sqrt{(k_\infty^2 - p^2)}]^* = \sqrt{(k_\infty^{*2} - p^2)} = |k_\infty^2 - p^2|^{\frac{1}{2}} \mathrm{e}^{-\mathrm{j}\alpha}, \tag{A 5}$$

which has branch points at $p = \pm k_\infty^*$. The important point to note in (A 5) is that the term $p^2$ under the second radical is not conjugated. Now, along the real axis, since $p = p^*$, (A 5) is clearly correct provided $\alpha = \theta$, for then $\zeta$ and $\eta$ are conjugates as required. It follows that, since the path of integration is along the real axis, the integral $I_{12}$ can be expressed as

$$I_{12} = \int_0^\infty p \frac{H_\mu^{(1)}(\eta z_1) H_{\mu^*}^{(2)}(\zeta z_2)}{H_\mu^{(1)}(\eta z_s) H_{\mu^*}^{(2)}(\zeta z_s)} \mathrm{d}p, \tag{A 6}$$

where $\eta$ and $\zeta$ are as defined in (A 3) and (A 5), respectively. The integrand in (A 6) is analytic throughout the complex $p$-plane (except at the poles and branch points). Therefore the integral $I_{12}$, as formulated in (A 6), can be evaluated by contour integration in the $p$-plane, even though off the real axis $\eta$ and $\zeta$ do not form a conjugate pair.

In the absence of absorption in the ocean (i.e. when the imaginary part of $k_\infty$ is identically zero) the two Hankel functions, of the first and second kind, in the denominator of the integrand in (A 6) show the same zeros, all of which fall on the real axis. Thus, the integral diverges through the presence of second-order poles on the path of integration (Olbers' paradox). These poles are converted to first order by allowing for attenuation in the medium, in which case the wavenumber, $k_\infty$, is complex, with imaginary part equal to $\beta > 0$. This has the effect of separating each second-order pole into two conjugate first-order poles, which fall either side of the real axis. This eliminates the problem of divergence in (A 6).

At all frequencies of interest in connection with propagating noise (say below 100 kHz), $\beta$ is several orders of magnitude smaller than the real part of $k_\infty$. Throughout most of the analysis of (A 6), $\beta$ is therefore insignificant and $k_\infty$ may be treated as real. It is only in handling the residues of the poles that $\beta$ must be included explicitly, to prevent the modal component of the noise from diverging.

Figure 13 shows the loci of the conjugate poles (first and fourth quadrants), along with the branch cuts associated with $\eta$ and $\zeta$ and the phases $\theta$ and $\alpha$, in the complex $p$-plane. The branch cuts are chosen to satisfy the conditions that $\mathrm{Im}\,(\eta) < 0$ and





PHILOSOPHICAL TRANSACTIONS OF THE ROYAL SOCIETY A MATHEMATICAL, PHYSICAL & ENGINEERING SCIENCES

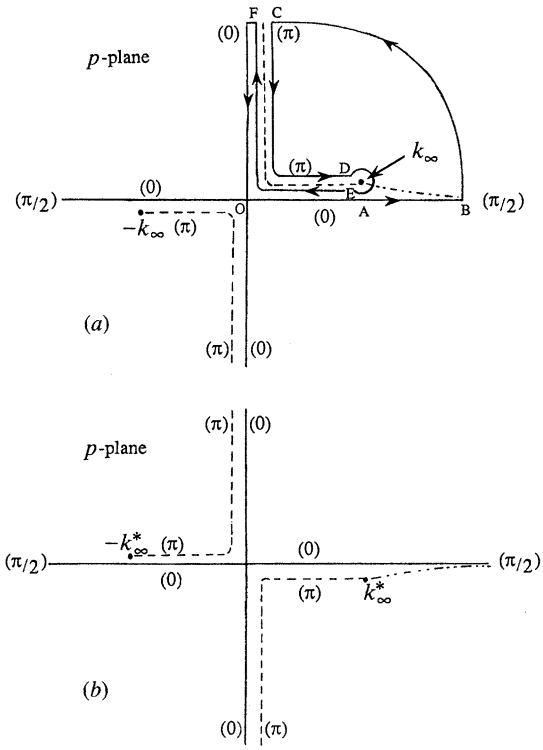


Figure 13. (*a*) Branch cuts of $\eta$, depicted by the dashed line, with values of the phase $\theta$ shown in brackets. The dash–dot–dot–dash line is the locus of the poles associated with the Hankel function $H_\mu^{(1)}(\eta z_s)$ in the integrand of (A 6). The arrows depict the contour used for the integration of $I_{12}$. (*b*) Branch cuts of $\zeta$, depicted by the dashed line, with values of the phase $\alpha$ shown in brackets. Notice that $\theta = \alpha$ along the real axis. The dash–dot–dot–dash line is the locus of the poles associated with the Hankel function $H_{\mu^*}^{(2)}(\zeta z_s)$ in the integrand of (A 6).

$\mathrm{Im}\,(\zeta) > 0$ everywhere on the top Riemann sheet (Felsen & Marcuvitz 1973), since these inequalities ensure convergence of the quotient of Hankel functions in (A 1) throughout the $p$-plane. It is evident from the phases in the diagram that $\eta$ and $\zeta$ do form a conjugate pair on the real axis but not elsewhere.

The closed contour to be used in performing the integration (figure 13) runs along the positive real axis (O → A → B), loops around at infinite radius (B → C), enclosing the poles in the first quadrant, runs around the branch cut (C → D → E → F) and back down the imaginary axis to the origin (F → O). Along the infinite loop, the integral is zero because of the above mentioned conditions on the imaginary parts of $\eta$ and $\zeta$, and hence the integral in (A 6) can be written as

$$I_{12} = \int_{\mathrm{O}\to\mathrm{A}} - \int_{\mathrm{C}\to\mathrm{D}} + 2\pi \mathrm{j} \sum_{m=0}^{\infty} R_m, \tag{A 7}$$

where $R_m$ is the residue of the $m$th pole in the first quadrant. The contributions from E → F and F → O → A cancel and there is a zero contribution from the circle of infinitesimal radius around the branch point itself. Now, on the right side of the branch cut, along the path C → D, the phase of $\eta$ is $\pi$, whereas the phase of $\zeta$ is zero. It follows that along the path C → D we have $\zeta = -\eta$, and hence on making a change of variable from $p$ to $\eta$ in the integral over the path C → D we obtain

$$I_{12} = L_1 - L_2 + L_3, \tag{A 8}$$

where

$$L_1 = \int_0^{k_\infty} \eta \frac{H^{(1)}_{-\mathrm{j}\nu}(\eta z_1) H^{(2)}_{-\mathrm{j}\nu}(\eta z_2)}{H^{(1)}_{-\mathrm{j}\nu}(\eta z_\mathrm{s}) H^{(2)}_{-\mathrm{j}\nu}(\eta z_\mathrm{s})} \mathrm{d}\eta, \tag{A 9a}$$

$$L_2 = \int_0^{\infty} \eta \frac{H^{(2)}_{-\mathrm{j}\nu}(\eta z_1) H^{(2)}_{\mathrm{j}\nu}(\eta z_2)}{H^{(2)}_{-\mathrm{j}\nu}(\eta z_\mathrm{s}) H^{(2)}_{\mathrm{j}\nu}(\eta z_\mathrm{s})} \mathrm{d}\eta, \tag{A 9b}$$

and

$$L_3 = 2\pi\mathrm{j} \sum_{m=0}^{\infty} R_m. \tag{A 9c}$$

In the first two of these equations, the order of the Hankel functions, $\mu$, has been set equal to $-\mathrm{j}\nu$, as in (22); and the process of analytic continuation (Abramowitz & Stegun 1965) has been used where necessary to ensure that all the Hankel functions have positive arguments.

The residue $R_m$ falls at $p = p_m$, where

$$p_m = \sqrt{(k_\infty^2 z_\mathrm{s}^2 + \sigma_m^2)}/z_\mathrm{s} \tag{A 10}$$

and $\sigma_m$ is the $m$th root of the characteristic equation

$$H^{(1)}_{-\mathrm{j}\nu}(\sigma) = 0. \tag{A 11}$$

As discussed in I, this equation has only real roots; and it reduces, through the substitution of an appropriate asymptotic form, to a simpler transcendental equation (24), which may be solved for $\sigma_m$ using a straightforward iterative technique. By setting

$$\eta_m = \sqrt{(k_\infty^2 - p_m^2)} \tag{A 12a}$$

and

$$\zeta_m = \sqrt{(k_\infty^{*2} - p_m^2)}, \tag{A 12b}$$

the residue can be expressed as

$$R_m = p_m \frac{H^{(1)}_{-\mathrm{j}\nu}(\eta_m z_1) H^{(2)}_{\mathrm{j}\nu}(\zeta_m z_2)}{[H^{(1)}_{-\mathrm{j}\nu}(\eta z_\mathrm{s})]'_{p=p_m} H^{(2)}_{\mathrm{j}\nu}(\zeta_m z_s)}, \tag{A 13}$$

where the prime denotes differentiation with respect to $p$.

From the uniform asymptotic form in (26), the derivative of the Hankel function in (A 13) is found to be

$$[H^{(1)}_{-\mathrm{j}\nu}(\eta z_\mathrm{s})]'_{p=p_m} = (-1)^{m+1} \mathrm{j}\, \mathrm{e}^{-\nu\pi} 2 \sqrt{(2/\pi)}\, z_\mathrm{s}\, \sigma_m^{-2} \sqrt{(k_\infty^2 z_\mathrm{s}^2 + \sigma_m^2)}\, (\nu^2 - \sigma_m^2)^{\frac{1}{4}}. \tag{A 14}$$

The Hankel function of the second kind in the denominator of (A 13) shows a zero at $p = p_m^*$. On expanding $H^{(2)}_{\mathrm{j}\nu}(\zeta_m z_\mathrm{s})$ to first order in a Taylor series about $p_m^*$, and recognizing that for vanishingly small $\beta/|k_\infty|$ the coefficient of the first-order term is the conjugate of the expression on the right of (A 14), we find that at $p = p_m$

$$H^{(2)}_{\mathrm{j}\nu}(\zeta_m z_\mathrm{s}) = (p_m - p_m^*)\, (-1)^m \mathrm{j}\, \mathrm{e}^{-\nu\pi} 2 \sqrt{(2/\pi)}\, \sigma_m^{-2} z_\mathrm{s} \sqrt{(k_\infty^2 z_\mathrm{s}^2 + \sigma_m^2)}\, (\nu^2 - \sigma_m^2)^{\frac{1}{4}}. \tag{A 15}$$

It follows from (A 10), since $\sigma_m$ is real, that for $\beta/|k_\infty| \ll 1$,

$$p_m - p_m^* = 2\mathrm{j} k_\infty \beta / p_m = 2\mathrm{j} k_\infty z_\mathrm{s} \beta / \sqrt{(k_\infty^2 z_\mathrm{s}^2 + \sigma_m^2)}. \tag{A 16}$$

On combining (A 13) to (A 16), the expression for the mode sum, $L_3$, becomes

$$L_3 = -\frac{\mathrm{e}^{2\nu\pi}\pi^2}{8k_\infty \beta z_s^4} \sum_{m=1}^{\infty} \frac{\sigma_m^4}{\sqrt{(\nu^2-\sigma_m^2)}} H^{(1)}_{-\mathrm{j}\nu}(\mathrm{j}\sigma_m \xi_1) H^{(1)}_{-\mathrm{j}\nu}(\mathrm{j}\sigma_m \xi_2), \tag{A 17}$$

where $\xi_{1,2}$ are normalized sensor depths, as defined in (21).

The presence of the absorption coefficient, $\beta$, in the denominator of (A 17) is obviously the origin of the infinity in the cross-spectrum of the noise in a lossless ocean. Elsewhere in (A 17) $\beta$ is negligible and $k_\infty$ may be treated as real. When the above expressions for $L_1$, $L_2$ and $L_3$ are substituted into (A 8) for the integral $I_{12}$, we obtain immediately the formulation of the cross-spectral density given in (20).

## Appendix B. The special case of an isovelocity ocean

When $h = 0$ the expression for the sound speed in (1) is independent of the depth coordinate $z$ and hence, under this special condition, the inverse-square profile represents an isovelocity ocean. In this case, the general inverse-square result in (20) should reduce to the known form for the vertical cross-spectral density of surface generated ambient noise in an ocean whose sound speed is independent of depth. The following argument demonstrates that this requirement is indeed satisfied.

From (22) it follows that $\nu = \frac{1}{2}\mathrm{j}$ when $h = 0$. The characteristic equation (23) then has no roots, implying that the normal mode component of the noise, $L_3$, is identically zero. The remaining two components, $L_1$ and $L_2$, corresponding to the two integrals in (20), involve Hankel functions of order $\pm\mathrm{j}\nu = \pm\frac{1}{2}$, which can be expressed exactly in terms of elementary functions:

$$H^{(1)}_{\frac{1}{2}}(x) = -\mathrm{j}\sqrt{(2/\pi x)}\exp(\mathrm{j}x) \tag{B 1a}$$

and

$$\mathrm{j}H^{(2)}_{-\frac{1}{2}}(x) = H^{(2)}_{\frac{1}{2}}(x) = \mathrm{j}\sqrt{(2/\pi x)}\exp(-\mathrm{j}x). \tag{B 1b}$$

On substituting these identities into the two integrals in (20), we find that

$$L_1 = \frac{z_s}{\sqrt{(z_1 z_2)}} \int_0^{k_\infty} \eta \exp(-\mathrm{j}\eta\Delta)\,\mathrm{d}\eta, \tag{B 2a}$$

$$L_2 = \frac{z_s}{\sqrt{(z_1 z_2)}} \int_0^{\infty} \eta \exp(-\mathrm{j}\eta a)\,\mathrm{d}\eta, \tag{B 2b}$$

where

$$\Delta = z_1 - z_2; \quad a = (z_1 + z_2 - 2z_s). \tag{B 3}$$

Both of the expressions in (B 2) can be evaluated analytically, the first by straightforward integration, which yields

$$L_1 = k_\infty^2 \frac{z_s}{\sqrt{(z_1 z_2)}} \left\{ \left[ \frac{\sin(k_\infty \Delta)}{k_\infty \Delta} + \frac{\cos(k_\infty \Delta) - 1}{(k_\infty \Delta)^2} \right] - \mathrm{j}\left[ \frac{\cos(k_\infty \Delta)}{k_\infty \Delta} - \frac{\sin(k_\infty \Delta)}{(k_\infty \Delta)^2} \right] \right\}. \tag{B 4}$$

This expression represents a downward travelling noise field, in which the noise power shows an (unique) angular dependence of the form $\cos(\phi)$, where $\phi$ is the vertical angle measured from the zenith. Such a directional density function is representative of a noise field generated by a surface distribution of dipoles (Buckingham 1990*a*).

Partial integration cannot be applied to the integral for $L_2$ because of convergence problems, but it can be evaluated with the aid of the theory of generalized functions.

The technique is to express the integrand as a derivative with respect to the parameter $a$ and then interchange the order of integration and differentiation:

$$L_2 = \frac{z_s}{\sqrt{(z_1 z_2)}} \int_0^\infty \eta \exp(-j a\eta)\, d\eta = j \frac{z_s}{\sqrt{(z_1 z_2)}} \frac{d}{da} \int_0^\infty \exp(-j a\eta)\, d\eta$$

$$= j \frac{z_s}{\sqrt{(z_1 z_2)}} \frac{d}{da} \left\{ \pi\delta(a) - \frac{j}{a} \right\} = j \frac{z_s}{\sqrt{(z_1 z_2)}} \left\{ -\pi \frac{\delta(a)}{a} + \frac{j}{a^2} \right\}$$

$$= -\frac{z_s}{\sqrt{(z_1 z_2)}} \frac{1}{a^2}, \tag{B 5}$$

where the delta function in the final expression has been omitted since it is zero whenever either sensor lies below the surface (i.e. when $a \neq 0$). The integration of the exponential function over semi-infinite limits in (B 5) has been performed using the properties of Fourier transforms (for the cosine component) and Hilbert transforms (for the sine component).

On combining the results in (B 4) and (B 5), the expression for the cross-spectral density of the noise in (20) reduces to

$$\langle S_{12}(\omega, z_1, z_2) \rangle = \rho Q(\omega) (k_\infty d')^2 / \pi$$

$$\times \left\{ \left[ \frac{\sin(k_\infty \Delta)}{k_\infty \Delta} + \frac{\cos(k_\infty \Delta) - 1}{(k_\infty \Delta)^2} \right] - j \left[ \frac{\cos(k_\infty \Delta)}{k_\infty \Delta} - \frac{\sin(k_\infty \Delta)}{(k_\infty \Delta)^2} \right] + \frac{1}{4 k_\infty^2 d^2} \right\}, \tag{B 6}$$

where $d = 2a$ is the mean depth (beneath the surface) of the two sensors. It is clear from (B 6) that $L_2$ represents a noise component that is spatially inhomogeneous but negligible at depths greater than a wavelength or so beneath the surface. The contribution from $L_1$, on the other hand, is spatially homogeneous since it involves only the sensor separation, $\Delta$, and not the sensor depths separately. The expression in (B 6) corresponds exactly with the known form for the (vertical) cross-spectral density of ambient noise in an isovelocity profile (Buckingham 1990*a*), thus providing a useful check on the general inverse-square result in (20).

## References


Abramowitz, M. & Stegun, I. A. 1965 *Handbook of mathematical functions*. New York: Dover.

Balogh, C. B. 1967 Asymptotic expansions of the modified Bessel function of the third kind of imaginary order. *SIAM J. appl. Math.* **15**, 1315–1323.

Buckingham, M. J. 1980 A theoretical model of ambient noise in a low-loss, shallow water channel. *J. Acoust. Soc. Am.* **67**, 1186–1192.

Buckingham, M. J. 1981 Spatial coherence of wind-generated noise in a shallow ocean channel. *J. Acoust. Soc. Am* **70**, 1412–1420.

Buckingham, M. J. 1983 *Noise in electronic devices and systems*. Chichester: Ellis Horwood.

Buckingham, M. J. 1985 A theoretical model of surface-generated noise in a wedge-shaped ocean with pressure-release boundaries. *J. Acoust. Soc. Am.* **78**, 143–148.

Buckingham, M. J. 1990*a* Infrasonic ambient noise in the ocean due to atmospheric pressure fluctuations on the surface. *J. Acoust. Soc. Am.* **88**, 984–994.

Buckingham, M. J. 1990*b* Ambient sound at the ice edge. In *Undersea Defence Technology Conference, Novotel, London, 7–9 February*, pp. 189–194.

Buckingham, M. J. 1991 On acoustic transmission in ocean-surface waveguides. *Phil. Trans. R. Soc. Lond.* A **335**, 513–555.






PHILOSOPHICAL TRANSACTIONS OF THE ROYAL SOCIETY A MATHEMATICAL, PHYSICAL & ENGINEERING SCIENCES

Buckingham, M. J., Berkhout, B. V. & Glegg, S. A. L. 1992 Imaging the ocean with ambient noise. *Nature, Lond.* **356**, 327–329.

Burgess, A. S. & Kewley, D. J. 1983 Wind-generated surface noise source levels in deep water east of Australia. *J. Acoust. Soc. Am.* **83**, 201–210.

Cox, H. 1973 Spatial correlation in arbitrary noise fields with application to ambient sea noise. *J. Acoust. Soc. Am.* **54**, 1289–1301.

Cron, B. F. & Sherman, C. H. 1962 Spatial correlation functions for various noise models. *J. Acoust. Soc. Am.* **34**, 1732–1736.

Cron, B. F. & Sherman, C. H. 1965 Spatial correlation functions for various noise models. *J. Acoust. Soc. Am.* **38**, 885(L).

Diachok, O. I. & Winokur, R. S. 1974 Spatial variability of underwater ambient noise at the Arctic ice-water boundary. *J. Acoust. Soc. Am.* **55**, 750–753.

Farmer, D. M. & Vagle, S. 1989 Waveguide propagation of ambient sound in the ocean-surface bubble layer. *J. Acoust. Soc. Am.* **86**, 1897–1908.

Felsen, L. B. & Marcuvitz, N. 1973 *Radiation and scattering of waves*, pp. 459–461. Englewood Cliffs: Prentice-Hall.

Isakovich, M. A. & Kur'yanov, B. F. 1970 Theory of low-frequency noise in the ocean. *Sov. Phys. Acoust.* **16**, 49–58.

Johannessen, O. M., Johannessen, J. A., Sandven, S. & Davidson, K. L. 1986 Preliminary results of the Marginal Ice Zone Experiment (MIZEX) summer operations. In *The Nordic Seas* (ed. Burton G. Hurdle), pp. 665–679. New York: Springer Verlag.

Kerman, B. R. 1988 *Sea Surface Sound*, NATO ASI Series. Dordrecht: Kluwer.

Kerman, B. R. 1993 *Natural physical sources of underwater sound*. Dordrecht: Kluwer.

Kibblewhite, A. C. & Hampton, L. D. 1980 A review of deep ocean sound attenuation data at very low frequencies. *J. Acoust. Soc. Am.* **67**, 147–157.

Kibblewhite, A. C., Shooter, J. A. & Watkins, S. L. 1976 Examination of attenuation at very low frequencies using the deep-water ambient noise field. *J. Acoust. Soc. Am.* **60**, 1040–1047.

Knudsen, V. O., Alford, R. S. & Emling, J. W. 1948 Underwater ambient noise. *J. mar. Res.* **7**, 410–429.

Kuperman, W. A. 1988 Propagation effects associated with ambient noise. In *Sea Surface Sound*, NATO ASI Series, pp. 253–272. Dordrecht: Kluwer.

Kuperman, W. A. & Ingenito, F. 1980 Spatial correlation of surface generated noise in a stratified ocean. *J. Acoust. Soc. Am.* **67**, 1988–1996.

Langer, R. E. 1932 On the asymptotic solutions of differential equations, with an application to the Bessel functions of large complex order. *Trans. Am. math. Soc.* **34**, 447–480.

Langer, R. E. 1949 The asymptotic solutions of ordinary linear differential equations of the second order, with special reference to a turning point. *Trans. Am. math. Soc.* **67**, 461–490.

Mackenzie, K. V. 1981*a* Discussion of sea water sound speed determinations. *J. Acoust. Soc. Am.* **70**, 801–806.

Mackenzie, K. V. 1981*b* Nine term equation for sound speed in the oceans. *J. Acoust. Soc. Am.* **70**, 807–812.

Meredith, R. W., Bucca, P. J. & McCoy, K. 1989 Environmental measurements and analysis: Arctic acoustics experiments in the Marginal Ice Zone. Naval Ocean Research and Development Activity, Report 210.

Minnaert, M. 1933 On musical air-bubbles and the sounds of running water. *Phil. Mag.* **16**, 235–248.

Olbers, H. W. M. 1826 Über die Durchsichtigkeit des Weltraumes. *Bode Jahrbuch* **110**. (Essentially the same article appeared in the February issue of *Bibliothèque Universelle*, and in the April–October issue of *Edin. New Phil. J.* **141**.)

Olver, F. W. J. 1974 *Asymptotics and special functions*. New York: Academic Press.

Pekeris, C. L. 1948 Theory of propagation of explosive sound in shallow water. *Geol. Soc. Am. Memo.* **27**, 1–117.

Perry, R. K. 1986 Bathymetry. In *The Nordic Seas* (ed. Burton G. Hurdle), pp. 211–234. New York: Springer Verlag.





PHILOSOPHICAL TRANSACTIONS OF THE ROYAL SOCIETY A MATHEMATICAL, PHYSICAL & ENGINEERING SCIENCES

Rice, S. O. 1944 Mathematical analysis of random noise. *Bell Syst. Tech. J.* **23**, 282–332.

Rice, S. O. 1945 Mathematical analysis of random noise. *Bell Syst. Tech. J.* **24**, 46–156.

Strasberg, M. 1979 Nonacoustic noise interference in measurements of infrasonic ambient noise. *J. Acoust. Soc. Am.* **65**, 1487–1493.

Thorp, W. H. 1965 Deep-ocean sound attenuation in the sub- and low-kilocycle per second region. *J. Acoust. Soc. Am.* **38**, 648–654.

Thorp, W. H. 1967 Analytic description of the low-frequency attenuation coefficient. *J. Acoust. Soc. Am.* **42**, 270.

Urick, R. J. 1983 *Principles of underwater sound*, 3rd edn. New York: McGraw-Hill.

Wadhams, P. 1986 The Ice Cover. In *The Nordic Seas* (ed. Burton G. Hurdle), pp. 20–84. New York: Springer Verlag.

Watkins, W. A., Tyack, P., Moore, K. E. & Bird, J. E. 1987 The 20 Hz signals of finback whales (*Balaenoptera physalus*). *J. Acoust. Soc. Am.* **82**, 1901–1912.

Wenz, G. M. 1962 Acoustic ambient noise in the ocean: spectra and sources. *J. Acoust. Soc. Am.* **34**, 1936–1956.

Wilson, J. H. 1983 Wind-generated noise modelling. *J. Acoust. Soc. Am.* **73**, 211–216.

*Received 23 April 1992; accepted 20 January 1993*





PHILOSOPHICAL TRANSACTIONS OF THE ROYAL SOCIETY A MATHEMATICAL, PHYSICAL & ENGINEERING SCIENCES